





RESEARCH ARTICLE | SEPTEMBER 20 2023

Optimal parameterizing manifolds for anticipating tipping points and higher-order critical transitions ^{EP}

Mickaël D. Chekroun  ; Honghu Liu ; James C. McWilliams 



Chaos 33, 093126 (2023)

<https://doi.org/10.1063/5.0167419>



CrossMark

AIP Advances

Why Publish With Us?

-  **25 DAYS**
average time to 1st decision
-  **740+ DOWNLOADS**
average per article
-  **INCLUSIVE**
scope

[Learn More](#)

Optimal parameterizing manifolds for anticipating tipping points and higher-order critical transitions

Cite as: Chaos 33, 093126 (2023); doi: 10.1063/5.0167419

Submitted: 12 July 2023 · Accepted: 31 August 2023 ·

Published Online: 20 September 2023



View Online



Export Citation



CrossMark

Mickaël D. Chekroun,^{1,a)}  Honghu Liu,²  and James C. McWilliams³ 

AFFILIATIONS

¹Department of Atmospheric and Oceanic Sciences, University of California, Los Angeles, California 90095-1565, USA and Department of Earth and Planetary Sciences, Weizmann Institute of Science, Rehovot 76100, Israel

²Department of Mathematics, Virginia Tech, Blacksburg, Virginia 24061, USA

³Department of Atmospheric and Oceanic Sciences and Institute of Geophysics and Planetary Physics, University of California, Los Angeles, California 90095-1565, USA

^{a)}Author to whom correspondence should be addressed: mcchekroun@atmos.ucla.edu

ABSTRACT

A general, variational approach to derive low-order reduced models from possibly non-autonomous systems is presented. The approach is based on the concept of optimal parameterizing manifold (OPM) that substitutes more classical notions of invariant or slow manifolds when the breakdown of “slaving” occurs, i.e., when the unresolved variables cannot be expressed as an exact functional of the resolved ones anymore. The OPM provides, within a given class of parameterizations of the unresolved variables, the manifold that averages out optimally these variables as conditioned on the resolved ones. The class of parameterizations retained here is that of continuous deformations of parameterizations rigorously valid near the onset of instability. These deformations are produced through the integration of auxiliary backward–forward systems built from the model’s equations and lead to analytic formulas for parameterizations. In this *modus operandi*, the backward integration time is the key parameter to select per scale/variable to parameterize in order to derive the relevant parameterizations which are doomed to be no longer exact away from instability onset due to the breakdown of slaving typically encountered, e.g., for chaotic regimes. The selection criterion is then made through data-informed minimization of a least-square parameterization defect. It is thus shown through optimization of the backward integration time per scale/variable to parameterize, that skilled OPM reduced systems can be derived for predicting with accuracy higher-order critical transitions or catastrophic tipping phenomena, while training our parameterization formulas for regimes prior to these transitions takes place.

© 2023 Author(s). All article content, except where otherwise noted, is licensed under a Creative Commons Attribution (CC BY) license (<http://creativecommons.org/licenses/by/4.0/>). <https://doi.org/10.1063/5.0167419>

We introduce a framework for model reduction to produce analytic formulas to parameterize the neglected variables. These parameterizations are built from the model’s equations in which only a scalar is left to calibrate per scale/variable to parameterize. This calibration is accomplished through a data-informed minimization of a least-square parameterization defect. By their analytic fabric, the resulting parameterizations benefit physical interpretability. Furthermore, our hybrid framework—analytic and data-informed—enables us to bypass the so-called extrapolation problem, known to be an important issue for purely data-driven machine-learned parameterizations. Here, by training our parameterizations prior to transitions, we are able to perform

accurate predictions of these transitions via the corresponding reduced systems.

I. INTRODUCTION

This article is concerned with the efficient reduction of forced-dissipative systems of the form

$$\frac{dy}{dt} = Ay + G(y) + F(t), \quad y \in H, \quad (1)$$

in which H denotes a Hilbert state space, possibly of finite dimension. The forcing term F is considered to be either constant in time or time-dependent, while A denotes a linear operator not necessarily self-adjoint,¹ which includes dissipative effects, and G denotes a nonlinear operator, which saturates the possible unstable growth due to unstable modes and may account for a loss of regularity (such as for nonlinear advection) in the infinite-dimensional setting. Such systems arise in a broad range of applications; see, e.g., Refs. 2–11.

The framework adopted is that of Ref. 12, which allows for deriving analytic parameterizations of the neglected scales that represent efficiently the nonlinear interactions with the retained, resolved variables. The originality of the approach of Ref. 12 is that the parameterizations are hybrid in their nature in the sense that they are both model-adaptive, based on the dynamical equations, and data-informed by high-resolution simulations.

For a given system, the optimization of these parameterizations benefits, thus, from their analytical origin resulting in only a few parameters to learn over short-in-time training intervals, mainly one scalar parameter per scale to parameterize. Their analytic fabric contributes to their physical interpretability compared to, e.g., parameterizations that would be machine learned. The approach is applicable to deterministic systems, finite- or infinite-dimensional, and is based on the concept of optimal parameterizing manifold (OPM) that substitutes the more classical notion of slow or invariant manifolds when there takes place a breakdown of “slaving” relationships between the resolved and unresolved variables,¹² i.e., when the latter cannot be expressed as an exact functional of the formers anymore.

By construction, the OPM takes its origin in a variational approach. The OPM is the manifold that averages out optimally the neglected variables as conditioned on the current state of the resolved ones, Refs. 12, Theorem 4. The OPM allows for computing approximations of the conditional expectation term arising in the Mori–Zwanzig approach to stochastic modeling of neglected variables;^{13–17} see also Theorem 5 in Ref. 12 as well as Refs. 18 and 19.

The approach introduced in Ref. 12 to determine OPMs, in practice, consists of first deriving analytic parametric formulas that match rigorous leading approximations of unstable/center manifolds or slow manifolds near, e.g., the onset of instability (Ref. 12, Sec. 2) and then to perform a data-driven optimization of the manifold formulas’ parameters to handle regimes further away from that instability onset (Ref. 12, Sec. 4). In other words, efficient parameterizations away from the onset are obtained as continuous deformations of parameterizations near the onset; deformations that are optimized by minimizing cost functionals tailored to the dynamics and measuring the defect of parameterization.

There, the optimization stage allows for alleviating the small denominator problems rooted in small spectral gaps and for improving the parameterization of small-energy but dynamically important variables. Thereby, relevant parameterizations are derived in regimes where constraining spectral gap or timescale separation conditions are responsible for the well-known failure of standard invariant/inertial or slow manifolds.^{12,20–25} As a result, the OPM approach provides (i) a natural remedy to the excessive backscatter transfer of energy to the low modes classically encountered in turbulence (Ref. 12, Sec. 6) and (ii) allows for deriving optimal

models of the slow motion for fast-slow systems not necessarily in the presence of timescale separation.^{18,19} Due to their optimal nature, OPMs allow also for providing accurate parameterizations of dynamically important small-energy variables; a well-known issue encountered in the closure of chaotic dynamics and related to (i).

This work examines the ability of the theory-guided and data-informed parameterization approach of Ref. 12 in deriving reduced systems able to predict higher-order transitions or catastrophic tipping phenomena, when the original, full system is possibly subject to time-dependent perturbations. From a data-driven perspective, this problem is tied to the so-called extrapolation problem, known, for instance, to be an important issue in machine learning, requiring more advanced methods such as, e.g., transfer learning.²⁶ While the past few decades have witnessed a surge and advances of many data-driven reduced-order modeling methodologies,^{27,28} the prediction of non-trivial dynamics for parameter regimes not included in the training dataset remains a challenging task. Here, the OPM approach by its hybrid framework—analytic and data-informed—allows us to bypass this extrapolation problem at a minimal cost in terms of learning efforts as illustrated in Secs. IV and V. As shown below, the training of OPMs at parameter values prior the transitions take place is sufficient to perform accurate predictions of these transitions via OPM reduced systems.

The remainder of this paper is organized as follows. We first survey in Sec. II the OPM approach and provide the general variational parameterization formulas for model reduction in the presence of a time-dependent forcing. We then expand in Sec. III on the backward–forward (BF) systems method^{12,29} to derive these formulas, clarifying fundamental relationships with homological equations arising in normal forms and invariant manifold theories.^{12,30–32} Section III C completes this analysis by analytic versions of these formulas in view of applications. The ability of predicting noise-induced transitions and catastrophic tipping phenomena^{33,34} through OPM reduced systems is illustrated in Sec. IV for a system arising in the study of thermohaline circulation. Successes in predicting higher-order transitions such as period-doubling and chaos are reported in Sec. V for a Rayleigh–Bénard problem, and contrasted by comparison with the difficulties encountered by standard manifold parameterization approaches in Appendix D. We then summarize the findings of this article with some concluding remarks in Sec. VI.

II. VARIATIONAL PARAMETERIZATIONS FOR MODEL REDUCTION

We summarize in this section the notion of variational parameterizations introduced in Ref. 12. The state space is decomposed as the sum of the subspace, H_c , of resolved variables (coarse-scale), and the subspace, H_s , of unresolved variables (small-scale). In practice, H_c is spanned by the first few eigenmodes of A with dominant real parts (e.g., unstable) and H_s by the rest of the modes, typically stable.

In many applications, one is interested in deriving reliable reduced systems of Eq. (1) for wavenumbers smaller than a cutoff scale k_c corresponding to a reduced state space H_c of dimension m_c . To do so, we are after parameterizations for the unresolved variables y_s [i.e., the vector component of the solution y to Eq. (1) in H_s] of

the form

$$\Phi_\tau(X, t) = \sum_{n \geq m_c+1} \Phi_n(\tau_n, X, t) e_n, \quad X \in H_c, \quad (2)$$

in which τ the (possibly infinite) vector formed by the scalars τ_n is a free parameter. As it will be apparent below, the goal is to get a small-scale parameterization which is not necessarily exact such that $y_s(t)$ is approximated by $\Phi_\tau(y_c(t), t)$ in a least-square sense, where y_c is the coarse-scale component of y in H_c . The vector τ is aimed to be a homotopic deformation parameter. The purpose is to have, as τ is varied, parameterizations that cover situations for which slaving relationships between the large and small scales hold ($y_s(t) = \Phi_\tau(y_c(t), t)$) as well as situations in which they are broken ($y_s(t) \neq \Phi_\tau(y_c(t), t)$), e.g., far from criticality. With the suitable τ , the goal is to dispose of a reduced system resolving only the “coarse-scales,” able to, e.g., predict higher-order transitions caused by nonlinear interactions with the neglected, “small-scales.”

As strikingly shown in Ref. 12, meaningful parameterizations away from the instability onset can still be obtained by relying on bifurcation and center manifold theories. To accomplish this feat, the parameterizations, rigorously valid near that onset, need though to be revisited as suitably designed continuous deformations. The *modus operandi* to provide such continuous deformations is detailed in Sec. III, based on the method of backward-forward systems introduced in Ref. 29, Chap. 4, in a stochastic context. In the case where $G(y) = G_k(y) + h.o.t$ with G_k a homogeneous polynomial of degree k , this approach gives analytical formulas of parameterizations given by (see Sec. III A)

$$\Phi_\tau(X, t) = \sum_{n \geq m_c+1} \left(\int_{-\tau_n}^0 e^{-s\lambda_n} \left(\Pi_n G_k(e^{sA_c} X - \eta(s)) + \Pi_n F(s+t) \right) ds \right) e_n, \quad (3)$$

with $X = \sum_{j=1}^{m_c} X_j e_j \in H_c$ and $\eta(s) = \int_s^0 e^{A_c(s-r)} \Pi_c F(r+t) dr$.

Here, (λ_n, e_n) denote the spectral elements of A which are ordered such that $\Re(\lambda_n) \geq \Re(\lambda_{n+1})$. In Eq. (3), Π_n and Π_c denote the projector onto $\text{span}(e_n)$ and $H_c = \text{span}(e_1, \dots, e_{m_c})$, respectively, while $A_c = \Pi_c A$. This formula provides an explicit expression for $\Phi_{\tau_n}^n(X, t)$ in (2) given here by the integral term over $[-\tau_n, 0]$ multiplying e_n in (3). The only free parameter per mode e_n to parameterize is the backward integration time τ_n .

The vector τ , made of the τ_n , is then optimized by using data from the full model. To allow for a better flexibility, the optimization is executed mode by mode one wishes to parameterize. Thus, given a solution $y(t)$ of the full model Eq. (1) over an interval I_T of length T , each parameterization $\Phi_{\tau_n}^n(X, t)$ of the solution amplitude $y_n(t)$ carried by mode e_n is optimized by minimizing—in the τ_n -variable—the following *parameterization defect*:

$$\mathcal{Q}_n(\tau_n, T) = \overline{|y_n(t) - \Phi_n(\tau_n, y_c(t), t)|^2}, \quad (4)$$

for each $n \geq m_c + 1$. Here, $\overline{(\cdot)}$ denotes the time-mean over I_T , while $y_n(t)$ and $y_c(t)$ denote the projections of $y(t)$ onto the high-mode e_n and the reduced state space H_c , respectively.

Geometrically, the function $\Phi_\tau(X, t)$ given by (3) provides a time-dependent manifold $\mathfrak{M}_\tau(t)$ such that

$$\overline{\text{dist}(y(t), \mathfrak{M}_\tau(t))^2} \leq \sum_{n=m_c+1}^N \mathcal{Q}_n(\tau_n, T), \quad (5)$$

where $\text{dist}(y(t), \mathfrak{M}_\tau(t))$ denotes the distance of $y(t)$ (lying, e.g., on the system’s global attractor) to the manifold \mathfrak{M}_τ .

Thus, minimizing each $\mathcal{Q}_n(\tau_n, T)$ (in the τ_n -variable) is a natural idea to enforce closeness of $y(t)$ in a least-squares sense to the manifold $\mathfrak{M}_\tau(t)$. Panel (a) in Fig. 1 illustrates (5) for the y_n -component: The optimal parameterization, $\Phi_n(\tau_n^*, X, t)$, minimizing (4) is shown for a case where the dynamics is transverse to it (e.g., in the absence of slaving), while $\Phi_n(\tau_n^*, X, t)$ provides the best parameterization in a least-squares sense.

In practice, the *normalized parameterization defect*, Q_n , is often used to compare different parameterizations. It is defined as $Q_n(\tau, T) = \mathcal{Q}_n(\tau, T)/|y_n|^2$. For instance, the flat manifold corresponding to no parameterization ($\tau_n = 0$) of the neglected variables (Galerkin approximations) comes with $Q_n = 1$ for all n , while a manifold corresponding to a perfect slaving relationship between $y_c(t)$ and $y_n(t)$ ’s, comes with $Q_n = 0$. When $0 < Q_n < 1$ for all n , the underlying manifold \mathfrak{M}_τ will be referred to as a *parameterizing manifold (PM)*. Once the parameters τ_n are optimized by minimization of (4), the resulting manifold will be referred to as the optimal parameterizing manifold (OPM).³⁵

We conclude this section by a few words of practical considerations. As documented in Ref. 12, Secs. 5 and 6, the amount of training data required in order to reach a robust estimation of the optimal backward integration time τ_n^* , is often comparable to the dynamics’ time horizon that is necessary to resolve the decay of correlations for the high-mode amplitude $y_n(t)$. For multiscale systems, one thus often needs to dispose of a training dataset sufficiently large to resolve the slowest decay of temporal correlations of the

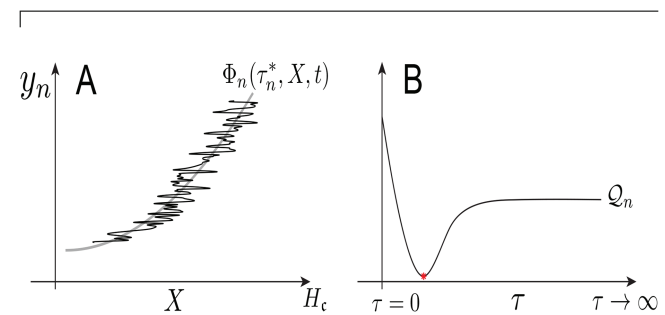


FIG. 1. Panel (a): The black curve represents the training trajectory, here shown to be transverse to the parameterizing manifolds (i.e., absence of exact slaving). The gray smooth curves represent the time-dependent OPM aimed at tracking the state of the neglected variable y_n at time t as a function of the resolved variables X . Panel (b): A schematic of the dependence on τ of the parameterization defect \mathcal{Q}_n given by (4). The red asterisk marks the minimum of \mathcal{Q}_n achieved for $\tau = \tau_n^*$.

scales to parameterize. On the other hand, by benefiting from their dynamical origin, i.e., through the model's equations, the parameterizations formulas employed in this study (see Sec. III) allow often for reaching out, in practice, satisfactory OPM approximations when optimized over training intervals shorter than these characteristic timescales.

When these conditions are met, the minimization of the parameterization defect (4) is performed by a simple gradient-descent algorithm (Ref. 12, Appendix). There, the first local minimum that one reaches corresponds often to the OPM; see Secs. IV and V and Ref. 12, Secs. 5 and 6. In the rare occasions where the parameterization defect exhibits more than one local minimum and the corresponding local minima are close to each others, criteria involving colinearity between the features to parameterize and the parameterization itself can be designed to further assist the OPM selection. Section V D illustrates this point with the notion of parameterization correlation.

III. VARIATIONAL PARAMETERIZATIONS: EXPLICIT FORMULAS

A. Homological equation and backward-forward systems: Time-dependent forcing

In this section, we recall from Ref. 12 and generalize to the case of time-dependent forcing, the theoretical underpinnings of the parameterization formula (3). First, observe that when $F \equiv 0$ and $\tau_n = \infty$ for all n , the parameterization (3) is reduced (formally) to

$$\mathfrak{J}(X) = \int_{-\infty}^0 e^{-sA_s} \Pi_s G_k(e^{sA_c} X) ds, \quad X \in H_c, \quad (6)$$

where $A_s = \Pi_s A$, with Π_s denoting the canonical projectors onto H_s . Equation (6) is known in invariant manifold theory as a Lyapunov–Perron integral.⁷ It provides the leading-order approximation of the underlying invariant manifold function if a suitable spectral gap condition is satisfied and solves the homological equation

$$D\psi(X)A_c X - A_s \psi(X) = \Pi_s G_k(X), \quad (7)$$

see Refs. 2, Lemma 6.2.4 and 12, Theorem 1. The later equation is a simplification of the invariance equation providing the invariant manifold when it exists; see Refs. 5, Sec. VIIA1 and 12, Sec. 2.2. Thus, Lyapunov–Perron integrals such as (6) are intimately related to the homological equation, and the study of the latter informs us on the former and, in turn, on the closed form of the underlying invariant manifold.

Another key element was pointed out in Ref. 29, Chap. 4, in the quest of getting new insights about invariant manifolds in general and more specifically concerned with the approximation of stochastic invariant manifolds of stochastic PDEs,³⁶ along with the rigorous low-dimensional approximation of their dynamics.³⁷ It consists of the method of backward–forward (BF) systems, thereafter revealed in Ref. 12 as a key tool to produce parameterizations (based on model's equations) that are relevant beyond the domain of applicability of invariant manifold theory, i.e., away the onset of instability.

To better understand this latter feature, let us recall first that BF systems allow for providing to Lyapunov–Perron integrals such

as (6), a flow interpretation. In the case of (6), this BF system takes the form [Ref. 12, Eq. (2.29)]

$$\frac{dp}{ds} = A_c p, \quad s \in [-\tau, 0], \quad (8a)$$

$$\frac{dq}{ds} = A_s q + \Pi_s G_k(p), \quad s \in [-\tau, 0], \quad (8b)$$

$$\text{with } p(s)|_{s=0} = X, \text{ and } q(s)|_{s=-\tau} = 0. \quad (8c)$$

The Lyapunov–Perron integral is indeed recovered from this BF system. The solution to Eq. (8b) at $s = 0$ is given by

$$q(0) = \int_{-\tau}^0 e^{-sA_s} \Pi_s G_k(e^{sA_c} X) ds, \quad X \in H_c, \quad (9)$$

which by taking the limit formally in (9) as $\tau \rightarrow \infty$ leads to \mathfrak{J} given by (6). Thus, stretching τ to infinity in the course of integration of the BF system (8) allows for recovering rigorous approximations (under some non-resonance conditions [Ref. 12, Theorem 1]) of well-known objects such as the center manifold; see also Refs. 2, Lemma 6.2.4 and 11, Appendix A.1. The intimate relationships between Lyapunov–Perron integral, $\mathfrak{J}(X)$, and the homological Eq. (7) are hence supplemented by their relationships with the BF system (8).

By breaking down, mode by mode, the backward integration of Eq. (8b) (in the case of A_s diagonal), one allows for a backward integration time τ_n per mode's amplitude to parameterize, leading, in turn, to the following class of parameterizations:

$$\Phi_\tau(X) = \sum_{n \geq m_c + 1} \left(\int_{-\tau_n}^0 e^{-sA_n} \Pi_n G_k(e^{sA_c} X) ds \right) e_n, \quad (10)$$

as indexed by $\tau = (\tau_n)_{n \geq m_c + 1}$. Clearly, Eq. (3) is a generalization of Eq. (10).

We make precise now the similarities and differences between Eqs. (3) and (10) at a deeper level as informed by their BF system representation. In that respect, we consider for the case of time-dependent forcing, the following BF system:

$$\frac{dp}{ds} = A_c p + \Pi_c F(s), \quad s \in [t - \tau, t], \quad (11a)$$

$$\frac{dq}{ds} = A_s q + \Pi_s G_k(p) + \Pi_s F(s), \quad s \in [t - \tau, t], \quad (11b)$$

$$\text{with } p(t) = X \in H_c \text{ and } q(t - \tau) = 0. \quad (11c)$$

Note that compared to the BF system (8), the backward–forward integration is operated here on $[t - \tau, t]$ to account for the non-autonomous character of the forcing, making this way the corresponding parameterization time-dependent as summarized in Lemma III.1. In the presence of an autonomous forcing, operating the backward–forward integration of the BF system (8) on $[t - \tau, t]$ does not change the parameterization, which remains time-independent.

Since the BF system (11) is one-way coupled [with p forcing (11b) but not reciprocally], if one assumes A_s to be diagonal

over \mathbb{C} , one can break down the forward equation (11b) into the equations

$$\frac{dq_n}{ds} = \lambda_n q_n + \Pi_n G_k(p) + \Pi_n F(s), \quad s \in [t - \tau, t], \quad (12)$$

allowing for flexibility in the choice of τ per mode e_n whose amplitude is aimed at being parameterized by q_n , for each $n \geq m_c + 1$.

After backward integration of Eq. (11a) providing $p(s)$, one obtains by forward integration of Eq. (12) that

$$q_n(t) = \int_{t-\tau}^t e^{(t-s')\lambda_n} \Pi_n G_k(e^{(s'-t)A_c} X - \gamma(s')) ds' + \int_{t-\tau}^t e^{(t-s')\lambda_n} \Pi_n F(s') ds', \quad (13)$$

with $\gamma(s') = \int_s^t e^{(s'-r)A_c} \Pi_c F(r) dr$. By making the change of variable $s' = s + t$, one gets

$$q_n(t) = \int_{-\tau}^0 e^{-s\lambda_n} \Pi_n G_k(e^{sA_c} X - \eta(s)) ds + \int_{-\tau}^0 e^{-s\lambda_n} \Pi_n F(s+t) ds, \quad (14)$$

with $\eta(s) = \int_s^0 e^{(s-r)A_c} \Pi_c F(r+t) dr = \gamma(s+t)$. Now, by summing up these parameterizations over the modes e_n for $n \geq m_c + 1$, we arrive at Eq. (3). Thus, our general parameterization formula (3) is derived by solving the BF system made of backward Eq. (11a) and the forward Eq. (12).

We want to gain into interpretability of such parameterizations in the context of forced-dissipative systems such as Eq. (1). For this purpose, we clarify the fundamental equation satisfied by our parameterizations; the goal being here to characterize the analog of (7) in this non-autonomous context. To simplify, we restrict to the case $\Pi_c F = 0$. The next lemma provides the sought equation.

Lemma III.1: Assume $\Pi_c F = 0$ in the BF system (11). The solution $q_{X,\tau}(t)$ to Eq. (11b) is given by

$$q_{X,\tau}(t) = \int_{-\tau}^0 e^{-sA_s} \Pi_s G_k(e^{sA_c} X) ds + \int_{-\tau}^0 e^{-sA_s} \Pi_s F(s+t) ds. \quad (15)$$

It provides a time-dependent manifold function that maps H_c into H_s and satisfies the following first order system of PDEs:

$$\begin{aligned} (\partial_t + \mathcal{L}_A)\Phi(X, t) &= \underbrace{\Pi_s G_k(X) - e^{\tau A_s} \Pi_s G_k(e^{-\tau A_c} X)}_{(I)} \\ &+ \underbrace{\Pi_s F(t) - e^{\tau A_s} \Pi_s F(t - \tau)}_{(II)}, \end{aligned} \quad (16)$$

with \mathcal{L}_A being the differential operator acting on smooth mappings ψ from H_c into H_s , defined as

$$\mathcal{L}_A[\psi](X) = D\psi(X)A_c X - A_s \psi(X), \quad X \in H_c. \quad (17)$$

The proof of this lemma is found in Appendix A.

As it will become apparent below, the τ -dependence of the terms in (I) is meant to control the small denominators that arise in the presence of small spectral gap between the spectrum of A_c

and A_s that leads typically to over-parameterization when standard invariant/inertial manifold theory is applied in such situations; see Remark III.1 and Ref. 12, Sec. 6.

The terms in (II) are responsible for the presence of exogenous memory terms in the solution to the homological equation Eq. (16), i.e., in the parameterization $\Phi(X, t)$; see Eq. (31).

In the case $F(t)$ is bounded,³⁸ and $\Re\sigma(A_s) < 0$, Eq. (16) reduces, in the (formal) limit $\tau \rightarrow \infty$, to

$$(\partial_t + \mathcal{L}_A)\Phi(X, t) = G_k(X) + \Pi_s F(t). \quad (18)$$

Such a system of linear PDEs is known as the homological equation and arises in the theory of time-dependent normal forms;^{31,39} see also Ref. 40. In the case where $\Pi_s F$ is T -periodic, one can seek an approximate solution in a Fourier expansion form (Ref. 41, Sec. 5.2), leading to useful insights. For instance, solutions to (18) when G is quadratic, exist if the following non-resonance condition is satisfied

$$i\nu \frac{\pi}{T} + \lambda_i + \lambda_j - \lambda_n \neq 0, \quad \nu \in \mathbb{Z}, \quad (19)$$

for $(i, j) \in I^2, n \geq m_c + 1$,

(with $I = \{1, \dots, m_c\}$ and $i^2 = -1$) in the case $\sigma(A)$ is discrete, without Jordan block. Actually, one can even prove in this case that

$$\text{Spec}(\partial_t + \mathcal{L}) = \left\{ i\nu \frac{\pi}{T} + \delta_{ij}^n, (i, j) \in I^2, n \geq m_c + 1, \nu \in \mathbb{Z} \right\}, \quad (20)$$

(where $\delta_{ij}^n = \lambda_i + \lambda_j - \lambda_n$) on the space of functions

$$\mathcal{E} = \left\{ \sum_{n \geq m_c + 1} \left(\sum_{i,j=1}^{m_c} \Gamma_{ij}^n(t) X_i X_j \right) e_n, \Gamma_{ij}^n \in L^2(\mathbb{T}) \right\}, \quad (21)$$

in which X_i and X_j represent the components of the vector X in H_c onto e_i and e_j , respectively.

Thus, in view of Lemma III.1 and what precedes, the small-scale parameterizations (15) obtained by solving the BF system (11) over finite time intervals can be conceptualized as perturbed solutions to the homological equation Eq. (18) arising in the computation of invariant and normal forms of non-autonomous dynamical systems Ref. 31, Sec. 2.2. The perturbative terms brought by the τ -dependence play an essential role to cover situations beyond the domain of application of normal form and invariant manifold theories. As explained in Sec. III C and illustrated in Secs. IV and V, these terms can be optimized to ensure skillful parameterizations for predicting, by reduced systems, higher-order transitions escaping the domain of validity of these theories.

B. Homological equation and backward-forward systems: Constant forcing

In this section, we clarify the conditions under which solutions to Eq. (11) exist in the asymptotic limit $\tau \rightarrow \infty$. We consider the case where F is constant in time, to simplify. For the existence of Lyapunov–Perron integrals under the presence of more general time-dependent forcings, we refer to Ref. 40. To this end, we

introduce, for X in H_c ,

$$\mathfrak{J}_F(X) = \int_{-\infty}^0 e^{-sA_s} (\Pi_s G_k(p(s)) + \Pi_s F) ds, \quad (22)$$

where $p(s)$ is the solution to Eq. (11a), namely,

$$p(s) = e^{sA_c} X - \int_s^0 e^{A_c(s-s')} \Pi_c F ds'. \quad (23)$$

We have then the following result that we cast for the case of finite-dimensional ODE system (of dimension N) to simply.

Theorem III.1: Assume that F is constant in time and that A is diagonal under its eigenbasis $\{e_j \in \mathbb{C}^N \mid j = 1, \dots, N\}$. Assume furthermore that $\Re(\lambda_{m_c+1}) < \Re(\lambda_{m_c})$ and $\Re\sigma(A_s) < 0$, i.e., H_s contains only stable eigenmodes.

Finally, assume that the following non-resonance condition holds:

$$\forall (j_1, \dots, j_k) \in (1, \dots, m_c)^k, n \geq m_c + 1, \quad (24)$$

$$(G_{j_1 \dots j_k}^n \neq 0) \implies \left(\Re \left(\lambda_n - \sum_{p=1}^k \lambda_{j_p} \right) < 0 \right),$$

with $G_{j_1 \dots j_k}^n = \langle G_k(e_{j_1}, \dots, e_{j_k}), e_n^* \rangle$, where $\langle \cdot, \cdot \rangle$ denotes the inner product on \mathbb{C}^N , G_k denotes the leading-order term in the Taylor expansion of G , and e_n^* denotes the eigenvectors of the conjugate transpose of A .

Then, the Lyapunov–Perron integral \mathfrak{J}_F given by (22) is well defined and is a solution to the following homological equation:

$$\mathcal{L}_A[\psi](X) + D\psi[X]\Pi_c F = \Pi_s G_k(X) + \Pi_s F \quad (25)$$

and provides the leading-order approximation of the invariant manifold function $h(X)$ in the sense that

$$\|\mathfrak{J}_F(X) - h(X)\|_{H_s} = o(\|X\|_{H_c}^k), \quad X \in H_c.$$

Moreover, \mathfrak{J}_F given by (22) is the limit, as τ goes to infinity, of the solution to the BF system (11), when F is constant in time. That is,

$$\lim_{\tau \rightarrow \infty} \|q_{X,\tau}(0) - \mathfrak{J}_F(X)\| = 0, \quad (26)$$

where $q_{X,\tau}(0)$ is the solution to Eq. (11b).

Conditions similar to (24) arise in the smooth linearization of dynamical systems near an equilibrium.⁴² Here, condition (24) implies that the eigenvalues of the stable part satisfy a Sternberg condition of order k^{42} with respect to the eigenvalues associated with the modes spanning the reduced state space H_c .

This theorem is essentially a consequence of Ref. 12, Theorems 1 and 2, in which condition (24) is a stronger version of that used for Ref. 12, Theorem 2; see also Ref. 12, Remark 1 (iv). This condition is necessary and sufficient here for $\int_{-\infty}^0 e^{-sA_s} \Pi_s G_k(p(s)) ds$ to be well defined. The convergence of $\int_{-\infty}^0 e^{-sA_s} \Pi_s F ds$ is straightforward since $\Re\sigma(A_s) < 0$ by assumption and F is constant. The derivation of (25) follows the same lines as the derivation for Ref. 12, Eq. (4.6).

One can also generalize Theorem III.1 to the case when F is time-dependent provided that F satisfies suitable conditions to

ensure \mathfrak{J}_F given by (22) to be well defined and that the non-resonance condition (24) is suitably augmented. We leave the precise statement of such a generalization to a future work. For the applications considered in later sections, the forcing term F is either a constant or with a sublinear growth. For such cases, \mathfrak{J}_F is always well defined under the assumptions of Theorem III.1. We turn now to present the explicit formulas of the parameterizations based on the BF system (11).

C. Explicit formulas for variational parameterizations

We provide in this section, closed form formulas of parameterizations for forced dissipative such as Eq. (1). We consider first the case where F is constant in time and then deal with time-dependent forcing case.

1. The constant forcing case

To favor flexibility in applications, we consider scale-awareness of our parameterizations via BF systems, i.e., we consider parameterizations that are built up, mode by mode, from the integration, for each $n \geq m_c + 1$, of the following BF systems:

$$\frac{dp}{ds} = A_c p + \Pi_c F, \quad s \in [-\tau, 0], \quad (27a)$$

$$\frac{dq_n}{ds} = \lambda_n q_n + \Pi_n G_k(p(s)) + \Pi_n F, \quad s \in [-\tau, 0], \quad (27b)$$

$$\text{with } p(0) = X \in H_c \text{ and } q_n(-\tau) = 0. \quad (27c)$$

Recall that $q_n(0)$ is aimed at parameterizing the solution amplitude $y_n(t)$ carried by mode e_n , when $X = y_c(t)$ in Eq. (27c), whose parameterization defect is minimized by optimization of the backward integration time τ in (4). To dispose of explicit formulas for $q_n(0)$ qualifying the dependence on τ facilitates greatly this minimization.

In the case the nonlinearity $G(y)$ is quadratic, denoted by $B(y, y)$, such formulas are easily accessible as (27) is integrable. It is actually integrable in the presence of higher-order terms, but we provide the details here for the quadratic case, leaving the details to the interested reader for extension.

Recall that we denote by e_j^* the conjugate modes from the adjoint A^* and that these modes satisfy the bi-orthogonality condition. That is $\langle e_i, e_j^* \rangle = 1$ if $i = j$, and zero otherwise, where $\langle \cdot, \cdot \rangle$ denotes the inner product endowing H . Denoting by $\Phi_n(\tau, \lambda, X)$ the solution $q_n(0)$ to Eq. (27b), we find after calculations that

$$\Phi_n(\tau, \lambda, X) = R_n(F, \lambda, \tau, X) - \frac{1 - e^{\tau\lambda_n}}{\lambda_n} F_n + \sum_{i,j=1}^{m_c} D_{ij}^n(\tau, \lambda) B_{ij}^n X_i X_j, \quad (28)$$

in which X_i and X_j denote the components of the vector X in H_c onto e_i and e_j , $B_{ij}^n = \langle B(e_i, e_j), e_n^* \rangle$ and

$$D_{ij}^n(\tau, \lambda) = \frac{1 - \exp(-\delta_{ij}^n \tau)}{\delta_{ij}^n}, \text{ if } \delta_{ij}^n \neq 0, \quad (29)$$

while $D_{ij}^n(\tau, \lambda) = \tau$ otherwise. Here, $\delta_{ij}^n = \lambda_i + \lambda_j - \lambda_n$, with the λ_j referring to the eigenvalues of A . We refer to Ref. 12 and Appendix B

for the expression of $R_n(F, \lambda, \tau, X)$, which accounts for the nonlinear interactions between the forcing components in H_c . Here, the dependence on the λ_j in (28) is made apparent, as this dependence plays a key role in the prediction of the higher-order transitions; see applications to the Rayleigh–Bénard system of Sec. V.

Remark III.1 (OPM balances small spectral gaps):

Theorem III.1 teaches us that when $\delta_{ij}^n > 0$ not only $D_{ij}^n(\tau, \lambda)$ defined in (29) converges toward a well-defined quantity as $\tau_n \rightarrow \infty$ but also the coefficients involved in $R_n(F, \lambda, \tau, X)$ [see (B1)–(B3)], in the case of existence of invariant manifold. For parameter regimes where the latter fails to exist, some of the δ_{ij}^n or the $\lambda_j - \lambda_n$ involved in (B2) and (B3) can become small, leading to the well-known small spectral gap issue²⁵ manifested typically by over-parameterization of the e_n 's mode amplitude when the Lyapunov–Perron parameterization (22) is employed; see Ref. 12, Sec. 6. The presence of the τ_n through the exponential terms in (29) and (B2) and (B3) allows for balancing these small spectral gaps after optimization and improve notably the parameterization and closure skills; see Sec. V and Appendix D.

Remark III.2: Formulas such as introduced in Ref. 43 in approximate inertial manifold (AIM) theory and used earlier in atmospheric dynamics⁴⁴ in the context of non-normal modes initialization^{45–47} are also tied to leading-order approximations of invariant manifolds since $\mathfrak{J}(X)$ given by (6) satisfies

$$\mathfrak{J}(X) = -A_s^{-1} \Pi_s G_k(X) + \mathcal{O}(\|X\|^k), \quad X \in H_c \quad (30)$$

and the term $-A_s^{-1} \Pi_s G_k(X)$ is the main parameterization used in Ref. 43; see Refs. 29, Lemma 4.1 and 11, Theorem A.1.1. Adding higher-order terms can potentially lead to more accurate parameterizations and push the validity of the approximation to a larger neighborhood,^{48,49} but in the presence of small spectral gaps, such an operation may become also less successful. When such formulas arising in AIM theory are inserted within the proper data-informed variational approach such as done in Ref. 12, Sec. 4.4, their optimized version can also handle regimes in which spectral gap becomes small as demonstrated in Ref. 12, Sec. 6.

2. The time-dependent forcing case

Here, we assume that the neglected modes are subject to time-dependent forcing according to $F(t) = \sum_{n \geq m_c+1} \sigma_n f_n(t) e_n$. Then, by solving the BF systems made of Eqs. (11a) and (12) with $q_n(t - \tau) = \zeta$ (to account for possibly non-zero mean), we arrive at the following time-dependent parameterization of the n th mode's amplitude:

$$\begin{aligned} \Phi_n(\tau, \lambda, X, t) = & e^{\lambda_n \tau} \zeta + \underbrace{\sigma_n e^{\lambda_n t} \int_{t-\tau}^t e^{-\lambda_n s} f_n(s) ds}_{(I)} \\ & + \sum_{ij=1}^{m_c} D_{ij}^n(\tau, \lambda) B_{ij}^n X_i X_j, \end{aligned} \quad (31)$$

where $X = \sum_{j=1}^{m_c} X_j e_j$ lies in H_c .

This formula of Φ_n gives the solution to the homological equation Eq. (16) of Lemma III.1 in which Π_s therein is replaced here by Π_n , the projector onto the mode e_n whose amplitude is parameterized by Φ_n . Clearly, the terms in (I) are produced by the

time-dependent forcing. They are functionals of the past f_n and convey thus *exogenous* memory effects.

The integral term in (I) of Eq. (31) is of the form

$$I(t) = e^{\kappa t} \int_{t-\tau}^t e^{-\kappa s} f_n(s) ds. \quad (32)$$

By taking derivatives on both sides of (32), we observe that I satisfies

$$\frac{dI}{dt} = \kappa I + f_n(t) - e^{\kappa \tau} f_n(t - \tau). \quad (33)$$

As a practical consequence, the computation of $I(t)$ boils down to solving the scalar ODE (33), which can be done with high-accuracy numerically, when $\kappa < 0$. One bypasses thus the computation of many quadratures (as t evolves) that we would have to perform when relying on Eq. (32). Instead, only one quadrature is required corresponding to the initialization of the ODE (33) at $t = 0$.

This latter computational aspect is important not only for simulation purposes when the corresponding OPM reduced system is ran online but also for training purposes, in the search of the optimal τ during the offline minimization stage of the parameterization defect.

If time-dependent forcing terms are present in the reduced state space H_c , then the BF system (27) can still be solved analytically albeit leading to more involved integral terms than in (I) in the corresponding parameterization. This aspect will be detailed elsewhere.

3. OPM reduced systems

Either in the constant forcing or time-dependent forcing case, our OPM reduced system takes the form

$$\dot{X} = A_c X + \Pi_c G(X + \Phi_{\tau^*}(X, t)) + \Pi_c F, \quad (34)$$

where

$$\Phi_{\tau}(X, t) = \sum_{n \geq m_c+1} \Phi_n(\tau_n, \lambda, X, t) e_n, \quad (35)$$

where either $\Phi_n(\tau_n, \lambda, X, t)$ is given by (31) in the time-dependent case, or by (28), otherwise. Whatever the case, the vector τ^* is formed by the minimizers τ_n^* of \mathcal{Q}_n given by (4), for each n . Note that in the case of the time-dependent parameterization (31), the OPM reduced system is run online by augmenting (35) with Eq. (33), depending on the modes that are forced.

We emphasize finally that from a data-driven perspective, the OPM reduced system benefits from its dynamical origin. By construction, only a scalar parameter τ is indeed optimized per mode to parameterize. This parameter benefits furthermore from a dynamical interpretation since it plays a key role in balancing the small spectral gaps known as to be the main issue in applications of invariant or inertial manifold theory in practice;²⁵ see Remark III.1.

IV. PREDICTING TIPPING POINTS

A. The Stommel–Cessi model and tipping points

A simple model for oceanic circulation showing bistability is Stommel's box model,⁵⁰ where the ocean is represented by two boxes, a low-latitude box with temperature T_1 and salinity S_1 , and

a high-latitude box with temperature T_2 and salinity T_2 ; see Ref. 51, Fig. 1. The Stommel model can be viewed as the simplest “thermodynamic” version of the Atlantic Meridional Overturning Circulation (AMOC) (Ref. 52, Chap. 6), a major ocean current system transporting warm surface waters toward the northern Atlantic that constitutes an important tipping point element of the climate system; see Refs. 53 and 54.

Cessi in Ref. 51 proposed a variation of this model, based on the box model of Ref. 55, consisting of an ODE system describing the evolution of the differences $\Delta T = T_1 - T_2$ and $\Delta S = S_1 - S_2$; see Ref. 51, Eq. (2.3). The Cessi model trades the absolute functions involved in the original Stommel model by polynomial relations more prone to analysis. The dynamics of ΔT and ΔS are coupled via the density difference $\Delta\rho$, approximated by the relation $\Delta\rho = \alpha_S \Delta S - \alpha_T \Delta T$ which induces an exchange Q of mass between the boxes to be given as $Q = 1/\tau_d + (q/V)\Delta\rho^2$ according to Cessi’s formulation, where q denotes the Poiseuille transport coefficient, V is the volume of a box, and τ_d is the diffusion timescale. The coefficient α_S is a coefficient inversely proportional to the practical salinity unit, i.e., unit based on the properties of sea water conductivity while α_T is in $^\circ\text{C}^{-1}$; see Ref. 51. In this simple model, ΔT relaxes at a rate τ , to a reference temperature θ (with $T_1 = \theta/2$ and $T_2 = -\theta/2$) in the absence of coupling between the boxes.

Using the dimensionless variables $y = \alpha_S \Delta S / (\alpha_T \theta)$, $z = \Delta T / \theta$, and rescaling time by the diffusion timescale τ_d , the Cessi model can be written as⁵⁶

$$\begin{aligned} \dot{y} &= F - y [1 + \mu(z - y)^2], \\ \dot{z} &= -\frac{1}{\epsilon}(z - 1) - z [1 + \mu(z - y)^2], \end{aligned} \quad (36)$$

in which F is proportional to the freshwater flux, $\epsilon = \tau_r / \tau_d$, and $\mu^2 = \tau_d (\alpha_T \theta)^2 q / V$; see Refs. 51, Eq. (2.6) and 56.

The nonlinear exchange of mass between the boxes is reflected by the nonlinear coupling terms in Eq. (36). These nonlinear terms lead to multiple equilibria in certain parts of the parameter space, in particular, when F is varied over a certain range $[F_{c1}, F_{c2}]$, while μ and ϵ are fixed. One can even prove that Eq. (36) experiences two saddle-node bifurcations,⁵⁷ leading to a typical S-shaped bifurcation diagram; see Fig. 2(a).

S-shaped bifurcation diagrams occur in oceanic models that go well beyond Eq. (36) such as based on the hydrostatic primitive equations or Boussinesq equations; see, e.g., Refs. 58–61. More generally, S-shaped bifurcation diagrams and more complex multiplicity diagrams are known to occur in a broad class of nonlinear problems^{62–64} that include energy balance climate models,^{65–68} population dynamics models,^{69,70} vegetation pattern models,^{71,72} combustion models,^{73–76} and many other fields.⁷⁷

The very presence of such S-shaped bifurcation diagrams provides the skeleton for tipping point phenomena to take place when such models are subject to the appropriate stochastic disturbances and parameter drift, causing the system to “tip” or move away from one branch of attractors to another; see Refs. 33 and 34. From an observational viewpoint, the study of tipping points has gained a considerable attention due to their role in climate change as a few components of the climate system (e.g., Amazon forest and the AMOC) have been identified as candidates for experiencing such critical transitions if forced beyond the point of no return.^{53,54,78}

Whatever the context, tipping phenomena are due to a subtle interplay between nonlinearity, slow parameter drift, and fast disturbances. To better understand how these interactions cooperate to produce a tipping phenomenon could help improve the design of

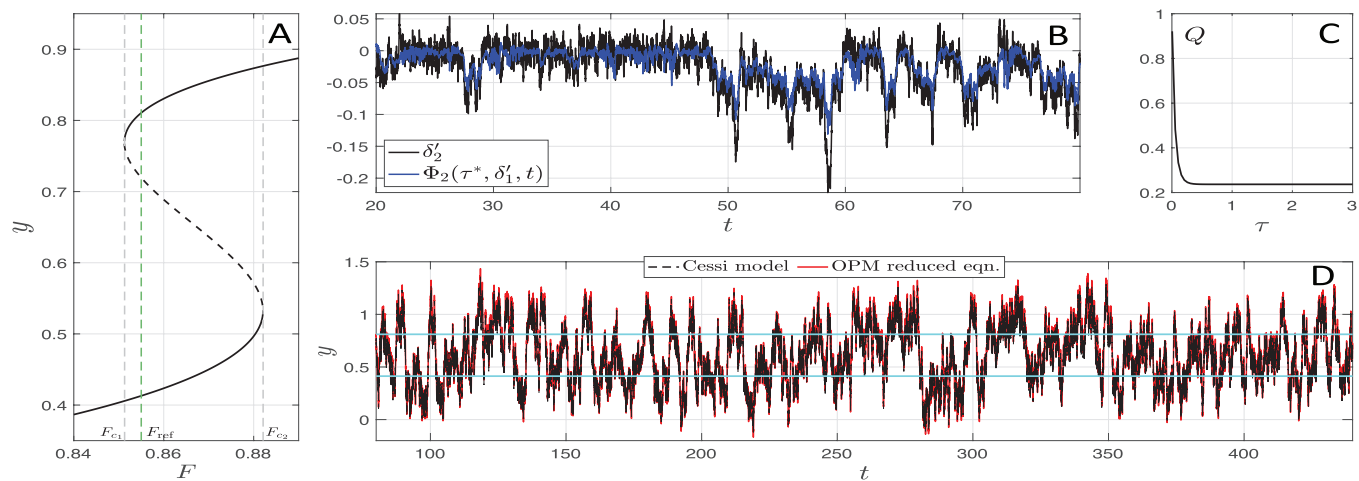


FIG. 2. Panel (a): The S-shaped bifurcation of the Stommel–Cessi model (36) as the parameter F is varied, shown here for $\mu = 6.2$ and $\epsilon = 0.1$. The two branches of locally stable steady states are marked by the solid black curves, and the other branch of unstable steady states are marked by the dashed black curve. The two vertical gray lines mark, respectively, $F_{c1} = 0.8513$ and $F_{c2} = 0.8821$, at which the saddle-node bifurcations occur. Panel (b): Parameterization of δ_2' by the OPM, $\Phi_2(\tau^*, \delta_1', t)$ given by (43), where F is fixed to be $F_{\text{ref}} = 0.855$ marked out by the vertical green line in panel (a) and the noise strength parameter σ in (40) is taken to be $\sigma = \sqrt{\epsilon}$, leading to $\sigma_1 \approx 0.3399$ and $\sigma_2 \approx -0.0893$ in (41). Panel (c): The normalized parameterization defect Q for $\Phi_2(\tau, \delta_1', t)$ as τ is varied. Panel (d): The performance of the OPM reduced Eq. (45) in reproducing the noise-induced transitions experienced by $y(t)$ from the stochastically forced Stommel–Cessi model (40). Once (45) is solved, the approximation of y is constructed using (46).

early warning signals. However, we will not focus on this latter point *per se* in this study, we show below, on the Cessi model that the OPM framework provides useful insights in that perspective, by demonstrating its ability of deriving reduced models to predict accurately the crossing of a tipping point; see Sec. IV C.

B. OPM results for a fixed F value: Noise-induced transitions

We report in this section on the OPM framework skills to derive accurate reduced models to reproduce noise-induced transitions experienced by the Cessi model (36), when subject to fast disturbances for a fixed value of F . The training of the OPM operated here serves as a basis for the harder tipping point prediction problem dealt with in Sec. IV C, when F is allowed to drift slowly through the critical value F_{c_2} at which the lower branch of steady

states experiences a saddle-node bifurcation manifested by a turning point; see Fig. 2(a) again. Recall that F_{c_1} denotes here the F -value corresponding to the turning point experienced by the upper branch.

Reformulation of the Cessi model (36). The 1D OPM reduced equation is obtained as follows. First, we fix an arbitrary value of F in $[F_{c_1}, F_{c_2}]$ that is denoted by F_{ref} and marked by the green vertical dashed line in Fig. 2(a). The system (36) is then rewritten for the fluctuation variables $y'(t) = y(t) - \bar{y}$ and $z'(t) = z(t) - \bar{z}$, where $\bar{X} = (\bar{y}, \bar{z})$ denotes the steady state of Eq. (36) in the lower branch when $F = F_{ref}$.

The resulting equation for $\delta = (y', z')$ is then of the form

$$\dot{\delta} = A\delta + G_2(\delta) + G_3(\delta), \tag{37}$$

with A, G_2, G_3 given by

$$A = \begin{pmatrix} -1 - \mu(\bar{z} - \bar{y})^2 + 2\mu\bar{y}(\bar{z} - \bar{y}) & -2\mu\bar{y}(\bar{z} - \bar{y}) \\ 2\mu\bar{z}(\bar{z} - \bar{y}) & -\frac{1}{\epsilon} - 1 - \mu(\bar{z} - \bar{y})^2 - 2\mu\bar{z}(\bar{z} - \bar{y}) \end{pmatrix}, \tag{38}$$

$$G_2(\delta) = \begin{pmatrix} -\mu\bar{y}(z' - y')^2 - 2\mu(\bar{z} - \bar{y})y'(z' - y') \\ -\mu\bar{z}(z' - y')^2 - 2\mu(\bar{z} - \bar{y})z'(z' - y') \end{pmatrix} \quad \text{and} \quad G_3(\delta) = \begin{pmatrix} -\mu y'(z' - y')^2 \\ -\mu z'(z' - y')^2 \end{pmatrix}. \tag{39}$$

Since \bar{X} is a locally stable steady state, we add noise to the first component of δ to trigger transitions from the lower branch to the top branch in order to learn an OPM that can operate not only locally near \bar{X} but also when the dynamics is visiting the upper branch. This leads to

$$\dot{\delta} = A\delta + G_2(\delta) + G_3(\delta) + \sigma \dot{W}(t), \tag{40}$$

where $\sigma = (\sigma, 0)^T$ and W denotes a standard one-dimensional two-sided Brownian motion.

The eigenvalues of A have negative real parts since \bar{X} is locally stable. We assume that the matrix A has two distinct real eigenvalues, which turns out to be the case for a broad range of parameter regimes. As in Sec. III, the spectral elements of the matrix A (respectively, A^*) are denoted by (λ_j, e_j) [respectively, (λ_j^*, e_j^*)], for $j = 1, 2$. These eigenmodes are normalized to satisfy $\langle e_j, e_j^* \rangle = 1$ and are bi-orthogonal otherwise.

Let us introduce $\delta' = (\langle \delta, e_1^* \rangle, \langle \delta, e_2^* \rangle)^T$ and $\sigma_j = \langle \sigma, e_j^* \rangle$, for $j = 1, 2$. We also introduce $\Lambda = \text{diag}(\lambda_1, \lambda_2)$. In the eigenbasis, Eq. (40) can be written then as

$$\dot{\delta}' = \Lambda \delta' + \mathcal{G}_2(\delta') + \mathcal{G}_3(\delta') + (\sigma_1 \dot{W}(t), \sigma_2 \dot{W}(t))^T, \tag{41}$$

with

$$\mathcal{G}_k^j(\delta') = \langle G_k(\delta'), e_j^* \rangle, \quad j = 1, 2, \tag{42}$$

where δ'_j denotes the j th component of δ' .

Derivation of the OPM reduced equation. We can now use the formulas of Sec. III C to obtain an explicit variational parameterization of the most stable direction carrying the variable δ'_2 here, in terms of the least stable one, carrying δ'_1 .

For Eq. (41), both of the forcing terms appearing in the p - and q -equations of the corresponding BF system (27) are stochastic (and thus time-dependent). To simplify, we omit the stochastic forcing in Eq. (27a) and work with the OPM formula given by (31) which, as shown below, is sufficient for deriving an efficient reduced system.

Thus, the formula (31) becomes in this context

$$\Phi_2(\tau, X, t) = D_{11}^2(\tau) B_{11}^2 X^2 + Z_\tau(t), \tag{43}$$

where D_{11}^2 is given by (29), $B_{11}^2 = \langle \mathcal{G}_2(e_1), e_2^* \rangle$, and

$$Z_\tau(t) = \sigma_2 e^{\lambda_2 t} \int_{t-\tau}^t e^{-\lambda_2 s} \dot{W}(s) ds. \tag{44}$$

Once the optimal τ^* is obtained by minimizing the parameterization defect given by (4), we obtain the following OPM reduced equation for δ'_1 :

$$\begin{aligned} \dot{X} = & \lambda_1 X + \left\langle G_2(Xe_1 + \Phi_2(\tau^*, X, t)e_2), e_1^* \right\rangle \\ & + \left\langle G_3(Xe_1 + \Phi_2(\tau^*, X, t)e_2), e_1^* \right\rangle + \sigma_1 \dot{W}(t). \end{aligned} \tag{45}$$

The online obtention of $X(t)$ by simulation of the OPM reduced equation Eq. (45) allows us to get the following approximation of

TABLE I. Parameter values.

ϵ	σ	μ	F_{c_1}	F_{c_2}	F_{ref}
0.1	$\sqrt{\epsilon}$	6.2	0.8513	0.8821	0.855

the variables $(y(t), z(t))$ from the original Cessi model (36):

$$(y_{\text{app}}(t), z_{\text{app}}(t))^T = X(t)e_1 + \Phi_2(\tau^*, X(t), t)e_2 + \bar{X}, \quad (46)$$

after going back to the original variables.

Numerical results. The OPM reduced equation Eq. (45) is able to reproduce the dynamics of δ'_1 for a wide range of parameter regimes. We show in Fig. 2 a typical example of skills for parameter values of μ, ϵ, σ , and $F = F_{\text{ref}}$ as listed in Table I. Since F_{ref} lies in $[F_{c_1}, F_{c_2}]$ (see Table I), the Cessi model (36) admits three steady states among which two are locally stable (lower and upper branches) and the other one is unstable (middle branch); see Fig. 2(a) again. For this choice of F_{ref} , the steady state corresponding to the lower branch is $\bar{X} = (\bar{y}, \bar{z})$ with $\bar{y} = 0.4130, \bar{z} = 0.8285$, and the eigenvalues of A are $\lambda_1 = -0.5168$ and $\lambda_2 = -15.7650$.

The offline trajectory $\delta'(t)$ used as input for training Φ_2 to find the optimal τ is taken as driven by an arbitrary Brownian path from Eq. (41) for t in the time interval $[20, 80]$. The resulting offline skills of the OPM, $\Phi_2(\tau^*, \delta'_1(t), t)$, are shown as the blue curve in Fig. 2(b), while the original targeted time series $\delta'_2(t)$ to parameterize is shown in black. The optimal τ that minimizes the normalized parameterization defect Q turns out to be ∞ for the considered regime, as shown in Fig. 2(c). One observes that the OPM captures, in average, the fluctuations of $\delta'_2(t)$; compare blue curve with black curve.

The skills of the corresponding OPM reduced Eq. (45) are shown in Fig. 2(d), after converting back to the original (y, z) -variable using (46). The results are shown out of sample, i.e., for another noise path and over a time interval different from the one used for training. The 1D reduced OPM reduced Eq. (45) is able to capture the multiple noise-induced transitions occurring across the two equilibria (marked by the cyan lines), after transforming back to the original (y, z) -variable; compare red with black curves in Fig. 2(d). Both the Cessi model (40) and the reduced OPM equation are numerically integrated using the Euler–Maruyama scheme with time step $\delta t = 10^{-3}$.

Note that we chose here the numerical value of F_{ref} to be closer to F_{c_1} than to F_{c_2} for making more challenging the tipping point prediction experiment conducted in Sec. IV C. There, we indeed train the OPM for $F = F_{\text{ref}}$ while aiming at predicting the tipping phenomenon as F drifts slowly through F_{c_2} (located thus further away) as time evolves.

C. Predicting the crossing of tipping points

OPM reduced Eq. (45) in the original coordinates. For better interpretability, we first rewrite the OPM reduced Eq. (45) under the original coordinates in which the Cessi model (36) is formulated. For that purpose, we exploit the components of the eigenvectors of A given by (38) (for $F = F_{\text{ref}}$) that we write as $e_1 = (e_{11}, e_{12})^T$ and

$e_2 = (e_{21}, e_{22})^T$. Then, from (46), the expression of y_{app} rewrites as

$$\begin{aligned} y_{\text{app}}(t) &= e_{11}X(t) + e_{21}\Phi_2(\tau^*, X(t), t) + \bar{y} \\ &= e_{11}X(t) + \gamma(\tau^*)X(t)^2 + e_{21}Z_{\tau^*}(t) + \bar{y}, \end{aligned} \quad (47)$$

where the second line is obtained by using the expression of Φ_2 given by (43) and the notation $\gamma(\tau^*) = e_{21}D_{11}^2(\tau^*)B_{11}^2$. It turns out that

$$\begin{aligned} X(t) &= \frac{-e_{11} + \sqrt{(e_{11})^2 - 4\gamma(\tau^*)(e_{21}Z_{\tau^*}(t) + \bar{y} - y_{\text{app}}(t))}}{2\gamma(\tau^*)} \\ &\stackrel{\text{def}}{=} \varphi(\tau^*, y_{\text{app}}(t), t), \quad t \geq 0. \end{aligned} \quad (48)$$

From (46), we also have

$$\begin{aligned} z_{\text{app}}(t) &= e_{12}X(t) + e_{22}\Phi_2(\tau^*, X(t), t) + \bar{z} \\ &= e_{12}X(t) + \gamma_2(\tau^*)X(t)^2 + e_{22}Z_{\tau^*}(t) + \bar{z}, \end{aligned} \quad (49)$$

where $\gamma_2(\tau^*) = e_{22}D_{11}^2(\tau^*)B_{11}^2$.

We can now express $z_{\text{app}}(t)$ as a function of $y_{\text{app}}(t)$, i.e., $z_{\text{app}}(t) = \Psi(\tau^*, y_{\text{app}}(t), t)$ with Ψ given by

$$\begin{aligned} \Psi(\tau^*, y_{\text{app}}, t) &= \bar{z} + \gamma_2(\tau^*)\varphi(\tau^*, y_{\text{app}}, t)^2 \\ &\quad + e_{12}\varphi(\tau^*, y_{\text{app}}, t) + e_{22}Z_{\tau^*}(t) \end{aligned} \quad (50)$$

as obtained by replacing $X(t)$ with $\varphi(\tau^*, y_{\text{app}}, t)$ in Eq. (49). Replacing y_{app} by the dummy variable y , one observes that Ψ provides a time-dependent manifold that parameterizes the variable z in the original Cessi model as (a time-dependent) polynomial function of radical functions in y due to the expression of $\varphi(\tau^*, y, t)$; see (48).

We are now in position to derive the equation satisfied by y_{app} aimed at approximating y in the original variables. For that purpose, we first differentiate with respect to time the expression of $X(t)$ given in (48) to obtain

$$\dot{X} = \frac{-e_{21}\dot{Z}_{\tau^*}(t) + \dot{y}_{\text{app}}}{\sqrt{(e_{11})^2 - 4\gamma(\tau^*)(e_{21}Z_{\tau^*}(t) + \bar{y} - y_{\text{app}})}}. \quad (51)$$

On the other hand, by taking into account the expressions of y_{app} in (47) and z_{app} in (49), we observe that the X -equation (45) can be re-written as

$$\dot{X} = \langle \mathcal{F}(y_{\text{app}}(t), z_{\text{app}}(t)) + \sigma \dot{W}(t), e_1^* \rangle. \quad (52)$$

with

$$\mathcal{F}(y, z) = \left(\begin{array}{c} F_{\text{ref}} - y[1 + \mu(z - y)^2] \\ -\frac{1}{\epsilon}(z - 1) - z[1 + \mu(z - y)^2] \end{array} \right), \quad (53)$$

given by the right-hand side (RHS) of the Cessi model (36) with $F = F_{\text{ref}}$.

Now, by equating the RHS of Eq. (52) with that of Eq. (51), we obtain, after substitution of z_{app} by $\Psi(\tau^*, y_{\text{app}}, t)$, that y_{app} satisfies

the following equation:

$$\dot{Y} = \alpha(\tau^*, Y) \left(\mathcal{F}(Y, \Psi(\tau^*, Y, t)) + \sigma \dot{W}(t), e_1^* \right) + e_{21} \dot{Z}_{\tau^*}(t), \quad (54)$$

where

$$\alpha(\tau^*, Y) = \sqrt{(e_{11})^2 - 4\gamma(\tau^*)(e_{21}Z_{\tau^*}(t) + \bar{y} - Y)}, \quad (55)$$

and \dot{Z}_{τ^*} is given by [cf. (44)]

$$\dot{Z}_{\tau^*}(t) = \lambda_2 Z_{\tau^*}(t) + \sigma_2 \dot{W}(t) - \sigma_2 e^{\lambda_2 \tau^*} \dot{W}(t - \tau^*). \quad (56)$$

Equation (54) is the OPM reduced equation for the y -variable of the Cessi model, as rewritten in the original system of coordinates. This equation in its analytic formulation mixes information about the two components of the RHS to Eq. (36) through the inner product involved in Eq. (54), while parameterizing the z -variable by the time-dependent parameterization $\Psi(\tau^*, \cdot, t)$ given by (50). While designed for $F = F_{\text{ref}}$ away from the lower tipping point, we show next that the OPM reduced system built up this way demonstrates a remarkable ability in predicting this tipping point when F is allowed to drift away from F_{ref} in the course of time.

Prediction results. Thus, we aim at predicting by our OPM reduced model, the tipping phenomenon experienced by the full model when F is subject to a slow drift in time via

$$F(t) = F_0 + \kappa t, \quad (57)$$

where $\kappa > 0$ is a small parameter, and F_0 is some fixed value of F such that $F_0 < F_{c_2}$, with F_{c_2} denoting the parameter value of the turning point of the lower branch of equilibria; see Fig. 2(a).

The original Cessi model is forced as follows:

$$\begin{aligned} \dot{y} &= F(t) - y[1 + \mu(z - y)^2] + \sigma \dot{W}_t, \\ \dot{z} &= -\frac{1}{\epsilon}(z - 1) - z[1 + \mu(z - y)^2]. \end{aligned} \quad (58)$$

Introducing $g(t) = \langle (F(t) - F_{\text{ref}}, 0)^T, e_1^* \rangle$ and writing $F(t)$ as $F_{\text{ref}} + (F(t) - F_{\text{ref}})$, we consider the following forced version of the OPM reduced Eq. (54):

$$\dot{Y} = \alpha(\tau^*, Y) \left(\mathcal{F}(Y, \Psi(\tau^*, Y, t)) + \sigma \dot{W}(t), e_1^* \right) + e_{21} \dot{Z}_{\tau^*}(t) + g(t). \quad (59)$$

In this equation, recall that the parameterization, $\Psi(\tau^*, \cdot, t)$ has been trained for $F = F_{\text{ref}}$; see above.

We set now $F_0 = 0.85$, $\kappa = 2 \times 10^{-4}$, and $\sigma = \sqrt{\epsilon}/50$, while $\mu = 6.2$ and $\epsilon = 0.1$ are kept as in Table I. Note that compared to the results shown in Fig. 2, the noise level is here substantially reduced to focus on the tipping phenomenon to occur in the vicinity of the turning point $F = F_{c_2}$. The goal is thus to compare the behavior of $y(t)$ solving the forced Cessi model (58) with that of the solution $Y(t)$ of the (forced) OPM reduced Eq. (59) as $F(t)$ crosses the critical value F_{c_2} .

The results are shown in Fig. 3. The red curve corresponds to the solution of the OPM reduced Eq. (59), and the black curve to the y -component of the forced Cessi model (58). Our baseline is the slow manifold parameterization, which consists of simply parameterizing z as $z = 1 + \mathcal{O}(\epsilon)$ in Eq. (59), which provides, for ϵ sufficiently

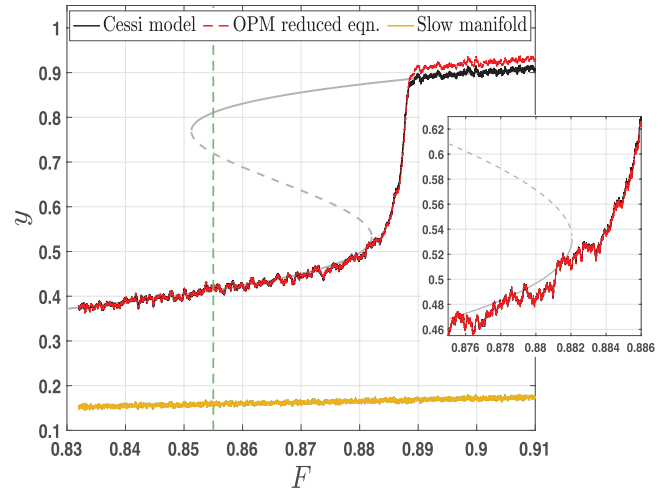


FIG. 3. The tipping phenomenon as predicted by the OPM reduced Eq. (59) (red curve) compared with that experienced by the full Cessi model (58) (black curve). The OPM is trained for $F = F_{\text{ref}} = 0.855$ as marked out by the vertical green line. Also shown in yellow is the result obtained from the slow manifold reduced Eq. (60).

small due to Tikhonov’s theorem,^{56,79} good reduction skills from the “slow” reduced equation

$$\dot{y} = F(t) - y[1 + \mu(1 - y)^2] + \sigma \dot{W}_t. \quad (60)$$

Here, the value $\epsilon = 0.1$ lies beyond the domain of applicability of the Tikhonov theorem, and as a result, the slow reduced Eq. (60) fails in predicting any tipping phenomenon; see yellow curve in Fig. 3. In contrast, the OPM reduced Eq. (59) demonstrates a striking success in predicting the tipping phenomenon to the upper branch, in spite of being trained away from the targeted turning point, for $F = F_{\text{ref}}$ as marked by the (green) vertical dash line. The only caveat is the overshoot observed in the magnitude of the predicted random steady state in the upper branch.

The striking prediction result of Fig. 3 are shown for one noise realization. We explore now the accuracy in predicting such a tipping phenomenon by the OPM reduced Eq. (59) when the noise realization is varied.

To do so, we estimate the statistical distribution of the F -value at which tipping takes place, denoted by $F_{\text{transition}}$, for both the Cessi model (58) and Eq. (59). These distributions are estimated as follows. We denote by \bar{y}_c the y -component of the steady state at which the saddle-node bifurcation occurs in the lower-branch for $F = F_{c_2}$. As noise is turned on and $F(t)$ evolves slowly through F_{c_2} , the solution path $y(t)$ to Eq. (58) increases in average while fluctuating around the \bar{y}_c -value (due to small noise) before shooting off to the upper branch as one nears F_{c_2} . During this process, there is a time instant, denoted by $t_{\text{transition}}$, such that for all $t > t_{\text{transition}}$, $y(t)$ stay above \bar{y}_c . We denote the F -value corresponding to $t_{\text{transition}}$ as $F_{\text{transition}}$ according to (57). Whatever the noise realization, the solution to the OPM reduced Eq. (59) experiences the same phenomenon leading thus to its own $F_{\text{transition}}$ for a particular noise realization. As shown by the histograms in Fig. 4, the distribution of $F_{\text{transition}}$ predicted

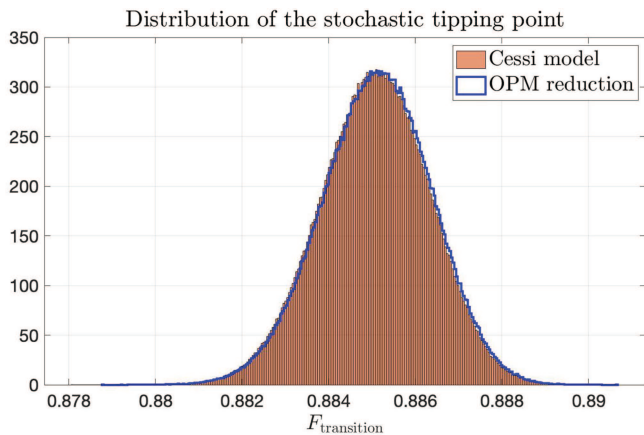


FIG. 4. Statistical distribution of the threshold value of F at which the tipping phenomenon occurs for both the full Cessi model (58) (orange bar) and the OPM reduced Eq. (59) (blue curve). The histograms are computed based on 10^6 arbitrarily fixed noise realizations.

by the OPM reduced Eq. (59) (blue curve) follows closely that computed from the full system (58) (orange bars). Thus, not only the OPM reduced Eq. (59) is qualitatively able to reproduce the passage through a tipping point (as shown in Fig. 3) but is also able to accurately predicting the critical F -value (or time-instant) at which the tipping phenomenon takes place with an overall success rate over 99%.

V. PREDICTING HIGHER-ORDER CRITICAL TRANSITIONS

A. Problem formulation

In this section, we aim at applying our variational parameterization framework to the following Rayleigh–Bénard (RB) system from Ref. 80:

$$\begin{aligned}
 \dot{C}_1 &= -\sigma b_1 C_1 - C_2 C_4 + b_4 C_4^2 + b_3 C_3 C_5 - \sigma b_2 C_7, \\
 \dot{C}_2 &= -\sigma C_2 + C_1 C_4 - C_2 C_5 + C_4 C_5 - \frac{\sigma}{2} C_9, \\
 \dot{C}_3 &= -\sigma b_1 C_3 + C_2 C_4 - b_4 C_2^2 - b_3 C_1 C_5 + \sigma b_2 C_8, \\
 \dot{C}_4 &= -\sigma C_4 - C_2 C_3 - C_2 C_5 + C_4 C_5 + \frac{\sigma}{2} C_9, \\
 \dot{C}_5 &= -\sigma b_5 C_5 + \frac{1}{2} C_2^2 - \frac{1}{2} C_4^2, \\
 \dot{C}_6 &= -b_6 C_6 + C_2 C_9 - C_4 C_9, \\
 \dot{C}_7 &= -b_1 C_7 - r C_1 + 2 C_5 C_8 - C_4 C_9, \\
 \dot{C}_8 &= -b_1 C_8 + r C_3 - 2 C_5 C_7 + C_2 C_9, \\
 \dot{C}_9 &= -C_9 - C_2(r + 2 C_6 + C_8) + C_4(r + 2 C_6 + C_7).
 \end{aligned}
 \tag{61}$$

Here, σ denotes the Prandtl number and r denotes the reduced Rayleigh number defined to be the ratio between the Rayleigh number R and its critical value R_c at which the convection sets in. The

TABLE II. Prediction experiments for the RB System (67). The parameter values r_D ($< r^*$) correspond to the allowable upper bound for which the mean state dependence of \bar{C}_r on r is estimated, in view of extrapolation at $r = r_p$. In each experiment, $I_r = [r_0, r_D]$ with $r_D - r_0 = 2 \times 10^{-2}$, corresponding to segments show in orange in Fig. 5(d). The critical value r^* indicates the parameter value at which the transition occurs, depending on the experiment. The parameter value $r_p > r^*$ at which the prediction is sought is also given.

	m_c	r_D	r^*	r_p
Experiment I (period-doubling)	3	13.91	13.99	14
Experiment II (chaos)	5	14.10	14.17	14.22

coefficients b_i are given by

$$\begin{aligned}
 b_1 &= \frac{4(1+a^2)}{1+2a^2}, & b_2 &= \frac{1+2a^2}{2(1+a^2)}, & b_3 &= \frac{2(1-a^2)}{1+a^2}, \\
 b_4 &= \frac{a^2}{1+a^2}, & b_5 &= \frac{8a^2}{1+2a^2}, & b_6 &= \frac{4}{1+2a^2},
 \end{aligned}$$

with $a = \frac{1}{2}$ corresponding to the critical horizontal wavenumber of the square convection cell. This system is obtained as a Fourier truncation of hydrodynamic equations describing Rayleigh–Bénard (RB) convection in a 3D box.⁸⁰ The Prandtl number is chosen to be $\sigma = 0.5$ in the experiments performed below, which is the same as used in Ref. 80. The reduced Rayleigh number r is varied according to these experiments; see Table II.

Our goal is to assess the ability of our variational parameterization framework for predicting higher-order transitions arising in (61) by training the OPM only with data prior to the transition we aim at predicting. The Rayleigh number r is our control parameter. As it increases, Eq. (67) undergoes several critical transitions/bifurcations, leading to chaos via a period-doubling cascade.⁸⁰ We focus on the prediction of two transition scenarios beyond Hopf bifurcation: (I) the period-doubling bifurcation and (II) the transition from a period-doubling regime to chaos. Noteworthy are the failures that standard invariant manifold theory or AIM encounter in the prediction of these transitions, here; see Appendix D.

To do so, we re-write Eq. (61) into the following compact form:

$$\dot{\mathbf{C}} = L\mathbf{C} + B(\mathbf{C}, \mathbf{C}), \tag{62}$$

where $\mathbf{C} = (C_1, \dots, C_9)^T$, and L is the 9×9 matrix given by

$$L = \begin{pmatrix}
 -\sigma b_1 & 0 & 0 & 0 & 0 & 0 & -\sigma b_2 & 0 & 0 \\
 0 & -\sigma & 0 & 0 & 0 & 0 & 0 & 0 & -\frac{\sigma}{2} \\
 0 & 0 & -\sigma b_1 & 0 & 0 & 0 & 0 & \sigma b_2 & 0 \\
 0 & 0 & 0 & -\sigma & 0 & 0 & 0 & 0 & \frac{\sigma}{2} \\
 0 & 0 & 0 & 0 & -\sigma b_5 & 0 & 0 & 0 & 0 \\
 0 & 0 & 0 & 0 & 0 & -b_6 & 0 & 0 & 0 \\
 -r & 0 & 0 & 0 & 0 & 0 & -b_1 & 0 & 0 \\
 0 & 0 & r & 0 & 0 & 0 & 0 & -b_1 & 0 \\
 0 & -r & 0 & r & 0 & 0 & 0 & 0 & -1
 \end{pmatrix}.$$

The nonlinear term B is defined as follows. For any $\phi = (\phi_1, \dots, \phi_9)^T$ and $\psi = (\psi_1, \dots, \psi_9)^T$ in \mathbb{C}^9 , we have

$$B(\phi, \psi) = \begin{pmatrix} -\phi_2\psi_4 + b_4\phi_4\psi_4 + b_3\phi_3\psi_5 \\ \phi_1\psi_4 - \phi_2\psi_5 + \phi_4\psi_5 \\ \phi_2\psi_4 - b_4\phi_2\psi_2 - b_3\phi_1\psi_5 \\ -\phi_2\psi_3 - \phi_2\psi_5 + \phi_4\psi_5 \\ \frac{1}{2}\phi_2\psi_2 - \frac{1}{2}\phi_4\psi_4 \\ \phi_2\psi_9 - \phi_4\psi_9 \\ 2\phi_5\psi_8 - \phi_4\psi_9 \\ -2\phi_5\psi_7 + \phi_2\psi_9 \\ -2\phi_2\psi_6 - \phi_2\psi_8 + 2\phi_4\psi_6 + \phi_4\psi_7 \end{pmatrix}. \quad (63)$$

We now re-write Eq. (61) in terms of fluctuations with respect to its mean state. In that respect, we subtract from $C(t) = (C_1(t), \dots, C_9(t))$ its mean state \bar{C}_r , which is estimated, in practice, from simulation of Eq. (61) over a typical characteristic time of the dynamics that resolves, e.g., decay of correlations (when the dynamics is chaotic) or a period (when the dynamics is periodic); see also Ref. 12. The corresponding ODE system for the fluctuation variable, $\delta(t) = C(t) - \bar{C}_r$, is then given by

$$\frac{d\delta}{dt} = A\delta + B(\delta, \delta) + L\bar{C}_r + B(\bar{C}_r, \bar{C}_r), \quad (64)$$

with

$$A\delta = L\delta + B(\bar{C}_r, \delta) + B(\delta, \bar{C}_r). \quad (65)$$

Denote the spectral elements of the matrix A by $\{(\lambda_j, e_j) : 1 \leq j \leq 9\}$ and those of A^* by $\{(\lambda_j^*, e_j^*) : 1 \leq j \leq 9\}$. Here the eigenmodes are normalized so that $\langle e_j, e_k^* \rangle = 1$ if $j = k$ and 0 otherwise. By taking the expansion of δ in terms of the eigenelements of L , we get

$$\delta(t) = \sum_{j=1}^9 y_j(t) e_j \quad \text{with} \quad y_j(t) = \langle \delta(t), e_j^* \rangle. \quad (66)$$

Assuming that A is diagonalizable in \mathbb{C} and by rewriting (64) in the variable $y = (y_1, \dots, y_9)^T$, we obtain that

$$\begin{aligned} \dot{y}_j &= \lambda_j(\bar{C}_r) y_j + \sum_{k,\ell=1}^9 B_{k\ell}^j(\bar{C}_r) y_k y_\ell + F_j(\bar{C}_r), \\ j &= 1, \dots, 9, \end{aligned} \quad (67)$$

where $B_{k\ell}^j(\bar{C}_r) = \langle B(e_k, e_\ell), e_j^* \rangle$ and

$$F_j(\bar{C}_r) = \langle L\bar{C}_r + B(\bar{C}_r, \bar{C}_r), e_j^* \rangle. \quad (68)$$

Like λ_j , the eigenmodes also depend on the mean state \bar{C}_r , explaining the dependence of the interaction coefficients $B_{k\ell}^j$. From now on, we work with Eq. (67).

B. Predicting higher-order transitions via OPM: Method

Thus, we aim at predicting for Eq. (67) two types of transition: (I) the period-doubling bifurcation and (II) the transition from period-doubling to chaos, referred to as Experiments I and II, respectively. For each of these experiments, we are given a reduced state space $H_c = \text{span}(e_1, \dots, e_{m_c})$ with m_c as indicated in Table II, depending on the parameter regime. The eignemodes are here ranked by the real part of the corresponding eigenvalues, e_1 corresponding to the eigenvalue with the largest real part. The goal is to derive an OPM reduced system (34) able to predict such transitions. The challenge lies in the optimization stage of the OPM due to the prediction constraint, one is prevented to use data from the full model at the parameter $r = r_p$ which one desires to predict the dynamics. Only data prior to the critical value r^* at which the concerned transition, either period-doubling or chaos takes place are here allowed.

Due to the dependence on \bar{C}_r of λ , as well as of the interaction coefficients $B_{k\ell}^j$ and forcing terms F_j , a particular attention to this dependence has to be paid. Indeed, recall that the parameterizations Φ_n given by the explicit formula (28) depend heavily here on the spectral elements of linearized operator A at \bar{C}_r and thus does its optimization. Since the goal is to eventually dispose of an OPM reduced system able to predict the dynamical behavior at $r = r_p > r^*$, one cannot rely on data from the full model at $r = r_p$ and thus one cannot exploit, in particular, the knowledge of the mean state \bar{C}_r for $r = r_p$. We are thus forced to estimate the latter for our purpose.

To do so, we estimate the dependence on r of \bar{C}_r on an interval $I_r = [r_0, r_D]$ such that $r_0 < r_D < r^*$ (see Table II), and use this estimation to extrapolate the value of \bar{C}_r at $r = r_p$, which we denote by $\bar{C}_{r_p}^{\text{ext}}$. For both experiments, it turned out that a linear extrapolation is sufficient. This extrapolated value $\bar{C}_{r_p}^{\text{ext}}$ allows us to compute the spectral elements of the operator A given by (65) in which $\bar{C}_{r_p}^{\text{ext}}$ replaces the genuine mean state \bar{C}_r . Obviously, the better is the approximation of \bar{C}_r by $\bar{C}_{r_p}^{\text{ext}}$, the better the approximation of $\lambda(\bar{C}_{r_p})$ by $\lambda(\bar{C}_{r_p}^{\text{ext}})$ along with the corresponding eigenspace.

We turn now to the training of the OPM exploiting these surrogate spectral elements, which will be used for predicting the dynamical behavior at $r = r_p$. To avoid any looking ahead whatsoever, we allow ourselves to only use the data of the full model (67) for $r = r_D < r_p$ and minimize the following parameterization defect:

$$\mathcal{J}_n(\tau) = \left| \overline{y_n^{r_D}(t) - \Phi_n(\tau, \lambda(\bar{C}_{r_p}^{\text{ext}}), y_c^{r_D}(t))} \right|^2, \quad (69)$$

for each relevant n , in which $y_c^{r_D}(t)$ (respectively, $y_n(t)$) denotes the full model solution's amplitude in H_c (respectively, e_n) at $r = r_D$. The normalized defect is then given by $J_n(\tau) = \mathcal{J}_n(\tau) / \overline{|y_n^{r_D}|^2}$. To compute these defects we proceed as follows. We first use the spectral elements at $r = r_p$ of the linearized matrix A at the extrapolated mean state $\bar{C}_{r_p}^{\text{ext}}$ to form the coefficients $R_n, \lambda_n^{-1} (1 - e^{\tau \lambda_n}) F_n$ and $D_{ij}^n(\tau, \lambda) B_{ij}^n$ involved in the expression (28) of Φ_n . For each n , the defect $\mathcal{J}_n(\tau)$ is then fed by the input data at $r = r_D$

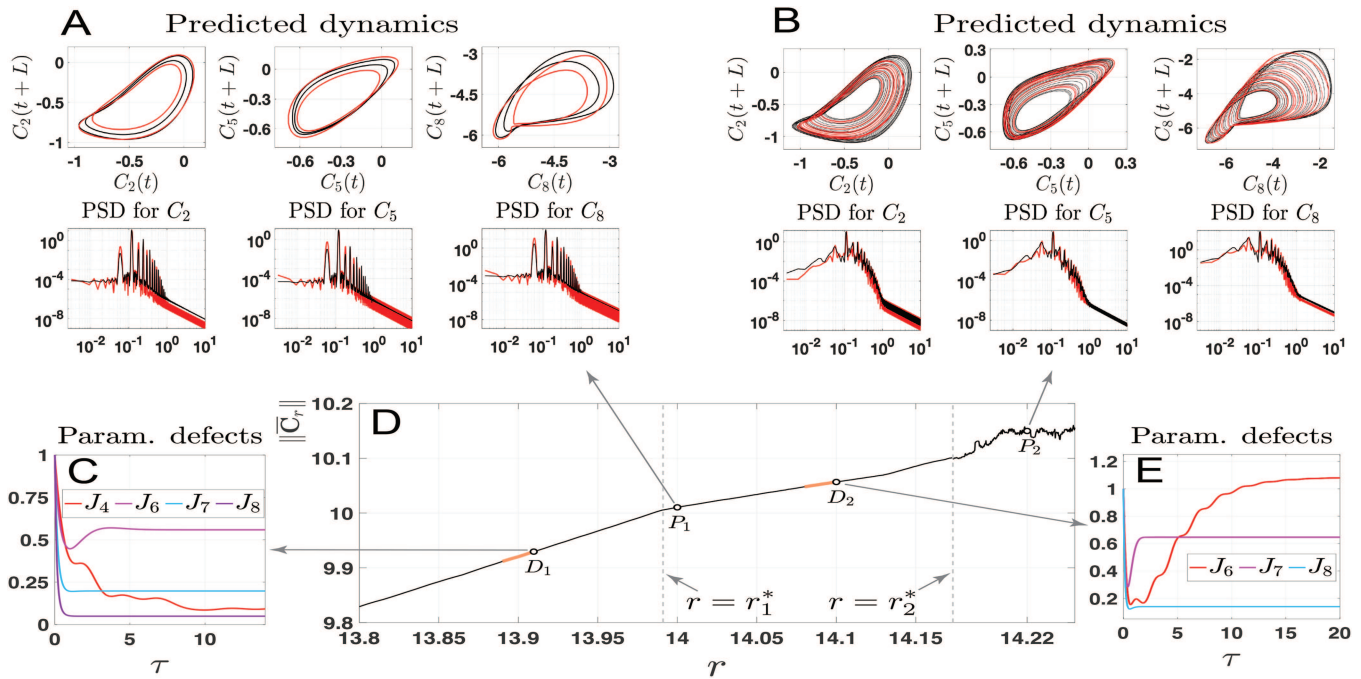


FIG. 5. Prediction of transitions: OPM prediction results. Panel (d): The black curve shows the dependence on r of the norm of the mean state vector, \bar{C}_r . The vertical dashed lines at $r_1^* = 13.991$ and $r_2^* = 14.173$ mark the onset of period-doubling bifurcation and chaos, respectively. The points P_1 and P_2 correspond to the r -values at which the two prediction experiments are conducted; see Table II. The orange segments that precede the points D_1 and D_2 denote the parameter intervals over which data are used to build the OPM reduced system for predicting the dynamics at $r = r_{P_1}$ and $r = r_{P_2}$, respectively; see Steps 1–4. The (normalized) parameterization defects are shown in panels (c) and (e) for training data at $r = r_{D_1}$ and $r = r_{D_2}$, respectively. Panels (a) and (b): Global attractor (in lagged coordinates) and PSDs for three selected components at $r = r_{P_1}$ and $r = r_{P_2}$, respectively. Black curves are from the full system (61), and red ones from the OPM reduced system (70).

[i.e., $y_n^{TD}(t)$ and $y_n^{D}(t)$] and evaluated for τ that varies in some sufficiently large interval to capture global minima. The results are shown in Figs. 5(c) and 5(e) for Experiment I and II, respectively. Note that the evaluation of $J_n(\tau)$ for a range of τ is used here only for visualization purposes as it is not needed to find a minimum. A simple gradient-descent algorithm can be indeed used for the latter; see Ref. 12, Appendix. We denote by $\hat{\tau}_n^*$ the resulting optimal value of τ per variable to parameterize.

After the $\hat{\tau}_n^*$ are found for each $n \geq m_c + 1$, the OPM reduced system used to predict the dynamics at $r = r_p$ takes the form

$$\begin{aligned} \dot{X}_j &= \hat{\lambda}_j(r_p)X_j + \sum_{k,\ell=1}^{m_c} \hat{B}_{k\ell}^j(r_p)X_kX_\ell \\ &+ \sum_{k=1}^{m_c} \sum_{\ell=m_c+1}^9 (\hat{B}_{k\ell}^j(r_p) + \hat{B}_{\ell k}^j(r_p))X_k\Phi_\ell(\hat{\tau}_\ell^*, \hat{\lambda}(r_p), X) \\ &+ \sum_{k,\ell=m_c+1}^9 \hat{B}_{k\ell}^j(r_p)\Phi_k(\hat{\tau}_k^*, \hat{\lambda}(r_p), X)\Phi_\ell(\hat{\tau}_\ell^*, \hat{\lambda}(r_p), X) \\ &+ \hat{F}_j(r_p), \quad j = 1, \dots, m_c, \end{aligned} \tag{70}$$

with $\hat{\lambda}_j(r_p) = \lambda_j(\bar{C}_{r_p}^{ext})$, $\hat{B}_{k\ell}^j(r_p) = B_{k\ell}^j(\bar{C}_{r_p}^{ext})$, and $\hat{F}_j(r_p) = F_j(\bar{C}_{r_p}^{ext})$.

We can then summarize our approach for predicting higher-order transitions via OPM reduced systems as follows:

- Step 1.** Extrapolation $\bar{C}_{r_p}^{ext}$ of \bar{C}_r at $r = r_p$ (the parameter at which one desires to predict the dynamics).
- Step 2.** Computation of the spectral elements of the linearized operator A at $r = r_p$ by replacing \bar{C}_r by $\bar{C}_{r_p}^{ext}$ in (65).
- Step 3.** Training of the OPM using the spectral elements of Step 2 and data of the full model for $r = r_D < r_p$.
- Step 4.** Run the OPM reduced system (70) to predict the dynamics at $r = r_p$.

We mention that the minimization of certain parameterization defects may require a special care such as for J_6 in Experiment II. Due to the presence of nearby local minima [see red curve in Fig. 5(e)], the analysis of the optimal value of τ to select for calibrating an optimal parameterization of $y_6(t)$ is more subtle and exploits actually a complementary metric known as the parameterization correlation; see Sec. V D.

Obviously, the accuracy in approximating the genuine mean state \bar{C}_{r_p} by \hat{C}_{r_p} is a determining factor in the transition prediction procedure described in steps 1–4 above. Here, the relative error in approximating $\|\bar{C}_{r_{P_i}}\|$ ($i = 1, 2$) is 0.03% for Experiment I and 0.27% for Experiment II. For the latter case, although the parameter

dependence is rough beyond r_2^* (see Panel D), there is no brutal local variations of relatively large magnitude as identified for other nonlinear systems.^{18,81} Systems for which a linear response to parameter variation is a valid assumption,^{82,83} thus constitute seemingly a favorable ground to apply the proposed transition prediction procedure.

C. Prediction of higher-order transitions by OPM reduced systems

As summarized in Figs. 5(a) and 5(b), for each prediction experiment of Table II, the OPM reduced system (70) not only successfully predicts the occurrence of the targeted transition at either $r = r_{p_1}$ and $r = r_{p_2}$ [P_1 and P_2 in Fig. 5(d)] but also approximates with good accuracy the embedded (global) attractor as well as key statistics of the dynamics such as the power spectral density (PSD). Note that for Experiment I (period-doubling), we choose the reduced dimension to be $m_c = 3$ and to be $m_c = 5$ for Experiment II (transition to chaos). For Experiment I, the global minimizers of $\mathcal{J}_n(\tau)$ given by (69) are retained to build up the corresponding OPM. In Experiment II, all the global minimizers are also retained except for $\mathcal{J}_6(\tau)$ from which the second minimizer is used for the construction of the OPM.

Once the OPM is built, an approximation of $C(t)$ is obtained from the solution $X(t)$ to the corresponding OPM reduced system (70) according to

$$C^{PM}(t) = \bar{C}_{r_p}^{ext} + \sum_{j=1}^{m_c} X_j(t)e_j + \sum_{n=m_c+1}^N \Phi_n(\hat{\tau}_n^*, \hat{\lambda}(r_p), X) e_n, \quad (71)$$

with Φ_n given by (28) whose spectral entries are given by the spectral elements of A given by (65) for $r = r_p$ in which \bar{C}_{r_p} is replaced by $\bar{C}_{r_p}^{ext}$. The e_j and e_n denote the eigenvectors of this matrix and $N = 9$ here.

As the baseline, the skills of the OPM reduced system (70) are compared to those from reduced systems when parameterizations from invariant manifold theory such as (6) or from inertial manifold theory such as (30), are employed; see Theorem 2 in Ref. 12 and Remark III.2. The details and results are discussed in Appendix D. The main message is that compared to the OPM reduced system (70), the reduced systems based on these traditional inertial/inertial manifold theories fail in predicting the correct dynamics. A main player in this failure lies in the inability of these standard parameterizations to accurately approximate small-energy variables that are dynamically important; see Appendix D. The OPM parameterization by its variational nature enables to fix this over-parameterization issue here.

D. Distinguishing between close local minima: Parameterization correlation analysis

Since Φ_n 's coefficients depend nonlinearly on τ [see Eqs. (28) and (29) and (B1)], the parameterization defects, $\mathcal{J}_n(\tau)$, defined in (69) are also highly nonlinear and may not be convex in the τ -variable as shown for certain variables in panels (c) and (e) of Fig. 5. A minimization algorithm to reach most often its global minimum is nevertheless detailed in Ref. 12, Appendix A and is not

limited to the RB system analyzed here. In certain rare occasions, a local minimum may be an acceptable halting point with an online performance slightly improved compared to that of the global minimum. In such a case, one discriminates between a local minimum and the global one by typically inspecting another metric offline: the correlation angle that measures essentially the collinearity between the actual high-mode dynamics and its parameterization. Here, such a situation occurs for Experiment II; see J_6 in Fig. 5(e).

Following Ref. 12, Sec. 3.1.2, we recall thus a simple criterion to assist the selection of an OPM when there are more than one local minimum displayed by the parameterization defect and the corresponding local minimal values are close to each other.

Given a parameterization Φ that is not trivial (i.e., $\Phi \neq 0$), we define the *parameterization correlation* as

$$c(t) = \frac{\text{Re}(\Phi(y_c(t)), y_s(t))}{\|\Phi(y_c(t))\| \|y_s(t)\|}. \quad (72)$$

It provides a measure of collinearity between the unresolved variable $y_s(t)$ and its parameterization $\Phi(y_c(t))$, as time evolves. It serves thus as a complimentary, more geometric way to measure the phase coherence between the resolved and unresolved variables than with the parameterization defect $\mathcal{Q}_n(\tau_n, T)$ defined in (4). The closer to unity $c(t)$ is for a given parameterization, the better phase coherence between the resolved and unresolved variables is expected to hold.

We illustrate this point on $J_6(\tau)$ shown in Fig. 5(e). The defect J_6 exhibits two close minima corresponding to $J_6 \approx 0.1535$ and $J_6 \approx 0.1720$, occurring respectively at $\tau \approx 0.65$ and $\tau \approx 1.80$. Thus, the parameterization defect alone does not help provide a satisfactory discriminatory diagnosis between these two minimizers. To the contrary, the parameterization correlation shown in Fig. 6 allows for diagnosing more clearly that the OPM associated with the local minimizer has a neat advantage compared to that associated with the global minimizer.

As explained in Ref. 12, Sec. 3.1.2, this parameterization correlation criterion is also useful to assist the selection of the dimension

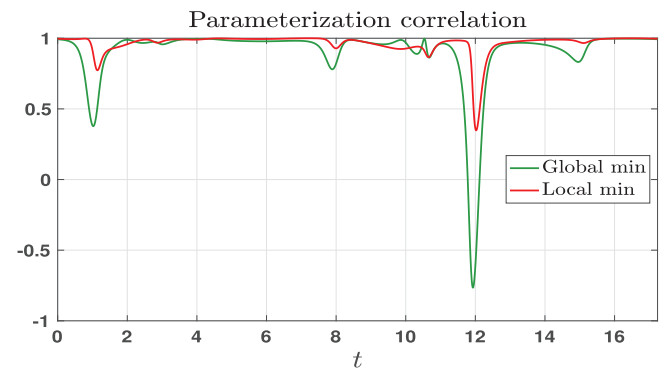


FIG. 6. Parameterization correlation $c(t)$ defined by (72) for the OPM in Experiment II (transition to chaos). The metric $c(t)$ is here computed by using the full model solutions for $r = r_D = 14.1$ in J_6 in (69), by making $\tau = 0.65$ and $\tau = 1.80$ corresponding to the global minimizer (green curve) and the nearby local minimizer (red curve), respectively; see Fig. 5(e).

of the reduced state space. Indeed, once an OPM has been determined, the dimension m_c of the reduced system should be chosen so that the parameterization correlation is sufficiently close to unity as measured, for instance, in the L^2 -norm over the training time window. The basic idea is that one should not only parameterize properly the statistical effects of the neglected variables but also avoid to lose their phase relationships with the unresolved variables.^{12,84} For instance, for predicting the transition to chaos, we observe that an OPM comes with a parameterization correlation much closer to unity in the case $m_c = 5$ than $m_c = 3$ (not shown).

VI. CONCLUDING REMARKS

In this article, we have described a general framework, based on the OPM approach introduced in Ref. 12 for autonomous systems, to derive effective (OPM) reduced systems that are able to predict either higher-order transitions caused by parameter regime shift or tipping phenomena caused by model's stochastic disturbances and slow parameter drift. In each case, the OPMs are sought as continuous deformations of classical invariant manifolds to handle parameter regimes away from bifurcation onsets while keeping the reduced state space relatively low-dimensional. The underlying OPM parameterizations are derived analytically from model's equations and constructed as explicit solutions to auxiliary BF systems such as Eq. (11), whose backward integration time is optimized per unresolved mode. This optimization involves the minimization of natural cost functionals tailored upon the full dynamics at parameter values prior to the transitions taking place; see (4). In each case—either for prediction of higher-order transitions or tipping points—we presented compelling evidence of the success of the OPM approach to address such extrapolation problems typically difficult to handle for data-driven reduction methods.

As reviewed in Sec. III, the BF systems such as Eq. (11) allow for drawing insightful relationships with the approximation theory of classical invariant/inertial manifolds (see Refs. 12, Sec. 2 and 31, 40, 85) when the backward integration time τ in Eq. (11) is sent to ∞ ; see Theorem III.1. Once the invariant/inertial manifolds fail to provide legitimate parameterizations, the optimization of the backward integration time may lead to local minima at finite τ of the parameterization defect, which if sufficiently small, gives access to skillful parameterizations to predict, e.g., higher-order transitions. This way, as illustrated in Sec. V (Experiment II), the OPM approach allows us to bypass the well-known stumbling blocks tied to the presence of small spectral gaps such as those encountered in inertial manifold theory²⁵ and tied to the accurate parameterization of dynamically important small-energy variables; see also Remark III.1, Appendix D, and Ref. 12, Sec. 6.

To understand the dynamical mechanisms at play behind a tipping phenomenon and to predict its occurrence are of uttermost importance, but this task is hindered by the often high dimensionality nature of the underlying physical system. Devising accurate and analytically reduced models to be able to predict tipping phenomenon from complex system is thus of prime importance to serve understanding. The OPM results of Sec. IV indicate great promises for the OPM approach to tackle this important task for more complex systems. Other reduction methods to handle the prediction of

tipping point dynamics have been proposed recently in the literature but mainly for mutualistic networks.^{86–88} The OPM formulas presented here are not limited to this kind of networks and can be directly applied to a broad class of spatially extended systems governed by (stochastic) PDEs or to nonlinear time-delay systems by adopting the framework of Ref. 89 for the latter to devise center manifold parameterizations and their OPM generalization; see Refs. 90 and 91.

The OPM approach could be also informative to design for such systems nearing a tipping point, early warning signal (EWS) indicators from multivariate time series. Extension of EWS techniques to multivariate data is an active field of research with methods ranging from empirical orthogonal functions reduction⁹² to methods exploiting the system's Jacobian matrix and relationships with the cross-correlation matrix⁹³ or exploiting the detection of spatial location of “hotspots” of stability loss.^{94,95} By its nonlinear *modus operandi* for reduction, the OPM parameterizations identify a subgroup of essential variables to characterize a tipping phenomenon which, in turn, could be very useful to construct the relevant observables of the system for the design of useful EWS indicators.

Thus, since the examples of Secs. IV and V are representative of more general problems of prime importance, the successes demonstrated by the OPM approach on these examples invites for further investigations for more complex systems.

Similarly, we would like to point out another important aspect in that perspective. For spatially extended systems, the modes involve typically wavenumbers that can help interpret certain primary physical patterns. Formulas such as (28) and (31) arising in OPM parameterizations involve a rebalancing of the interactions B_{ij}^n among such modes by means of the coefficients $D_{ij}^n(\tau, \lambda)$; see Remark III.1. Thus, an OPM parameterization when skillful to derive efficient systems may provide useful insights into explaining emergent patterns due to certain nonlinear interactions of wavenumbers for regimes beyond the instability onset. For more complex systems that are dealt with here, it is known already that near the instability onset of primary bifurcations, center manifold theory provides such physical insights; see, e.g., Refs. 96–102.

By the approach proposed here, relying on OPMs obtained as continuous deformations of invariant/center manifolds, one can thus track the interactions that survive or emerge between certain wavenumbers as one progresses through higher-order transitions. Such insights bring new elements to potentially explain the low-frequency variability of recurrent large-scale patterns typically observed, e.g., in oceanic models,^{103,104} offering at least new lines of thoughts to the dynamical system approach proposed in the previous studies.^{104–107} In that perspective, the analytic expression (B1) of terms such as $R_n(F, \lambda, \tau, X)$ in (28) bring also new elements to break down the nonlinear interactions between the forcing of certain modes compared to others. Formulas such as (B1) extend to the case of time-dependent or stochastic forcing of the coarse-scale modes whose exact expression will be communicated elsewhere. As for the case of noise-induced transitions reported in Fig. 2(d), these generalized formulas are expected to provide, in particular, new insights into regime shifts not involving crossing a bifurcation point but tied to other mechanisms such as slow–fast cyclic transitions or stochastic resonances.¹⁰⁸

Yet, another important practical aspect that deserves in-depth investigation is related to the robustness of the OPM approach subject to model errors. Such errors can arise from multiple sources, including, e.g., imperfection of the originally utilized high-fidelity model in capturing the true physics and noise contamination of the solution data used to train the OPM. For the examples of Secs. IV and V, since we train the OPM in a parameter regime prior to the occurrence of the concerned transitions, the utilized training data contain, *de facto*, model errors. The reported results in these sections show that the OPM is robust in providing effectively reduced models subject to such model errors. Nevertheless, it would provide useful insights if one can systematically quantify uncertainties of the OPM reduced models subject to various types of model errors. In that respect, several approaches could be beneficial for stochastic systems such as those based on the information-theoretic framework of Ref. 109 or the perturbation theory of ergodic Markov chains and linear response theory,¹¹⁰ as well as methods based on data-assimilation techniques.¹¹¹

ACKNOWLEDGMENTS

We are grateful to the reviewers for their constructive comments, which helped enrich the discussion and presentation. This work has been partially supported by the Office of Naval Research (ONR) Multidisciplinary University Research Initiative (MURI) Grant (No. N00014-20-1-2023), the National Science Foundation Grant (No. DMS-2108856), and the European Research Council (ERC) under the European Union’s Horizon 2020 research and innovation program (Grant Agreement No. 810370). We also acknowledge the computational resources provided by Advanced Research Computing at Virginia Tech for the results shown in Fig. 4.

AUTHOR DECLARATIONS

Conflict of Interest

The authors have no conflicts to disclose.

Author Contributions

Mickaël D. Chekroun: Conceptualization (equal); Formal analysis (equal); Funding acquisition (equal); Investigation (equal); Methodology (equal); Writing – original draft (equal). **Honghu Liu:** Conceptualization (equal); Formal analysis (equal); Funding acquisition (equal); Investigation (equal); Methodology (equal); Writing – original draft (equal). **James C. McWilliams:** Conceptualization (equal); Formal analysis (equal); Funding acquisition (equal); Investigation (supporting); Methodology (supporting); Writing – original draft (supporting).

DATA AVAILABILITY

The data that support the findings of this study are available from the corresponding author upon reasonable request.

APPENDIX A: PROOF OF LEMMA III.1

We introduce the notations

$$g_\tau(t) = \int_{-\tau}^0 e^{-sA_\mathfrak{s}} \Pi_\mathfrak{s} F(s+t) ds, \tag{A1}$$

$$\Psi_\tau(X) = \int_{-\tau}^0 e^{-sA_\mathfrak{s}} \Pi_\mathfrak{s} B(e^{sA_\mathfrak{c}} X) ds.$$

In Eq. (15), replacing X by $e^{rA_\mathfrak{c}} X$ where r is an arbitrary real number, we get

$$\Phi_\tau(e^{rA_\mathfrak{c}} X, t) = \Psi_\tau(e^{rA_\mathfrak{c}} X) + g_\tau(t). \tag{A2}$$

Note that

$$\begin{aligned} \varphi(r) &= \Psi_\tau(e^{rA_\mathfrak{c}} X) = \int_{-\tau}^0 e^{-sA_\mathfrak{s}} \Pi_\mathfrak{s} B(e^{(s+r)A_\mathfrak{c}} X) ds \\ &= \int_{r-\tau}^r e^{(r-s')A_\mathfrak{s}} \Pi_\mathfrak{s} B(e^{s'A_\mathfrak{c}} X) ds'. \end{aligned} \tag{A3}$$

We obtain then

$$\partial_r \varphi(r) = \Pi_\mathfrak{s} B(e^{rA_\mathfrak{c}} X) - e^{\tau A_\mathfrak{s}} \Pi_\mathfrak{s} B(e^{(r-\tau)A_\mathfrak{c}} X) + A_\mathfrak{s} \varphi(r). \tag{A4}$$

On the other hand, since $\varphi(r) = \Phi_\tau(e^{rA_\mathfrak{c}} X, t) - g_\tau(t)$ due to (15), we also have

$$\partial_r \varphi(r) = D\Phi_\tau(e^{rA_\mathfrak{c}} X, t) A_\mathfrak{c} e^{rA_\mathfrak{c}} X. \tag{A5}$$

By taking the limit $r \rightarrow 0$, we obtain from (A4) and (A5) that

$$D\Phi_\tau(X, t) A_\mathfrak{c} X = \Pi_\mathfrak{s} B(X) - e^{\tau A_\mathfrak{s}} \Pi_\mathfrak{s} B(e^{-\tau A_\mathfrak{c}} X) + A_\mathfrak{s} \Psi_\tau(X). \tag{A6}$$

Now, if we replace t in (15) by $t+r$, we obtain

$$\Phi_\tau(X, t+r) = \Psi_\tau(X) + g_\tau(t+r). \tag{A7}$$

Note that

$$\begin{aligned} \tilde{\varphi}(r) &= g_\tau(t+r) = \int_{-\tau}^0 e^{-sA_\mathfrak{s}} \Pi_\mathfrak{s} F(s+t+r) ds \\ &= \int_{r-\tau}^r e^{(r-s')A_\mathfrak{s}} \Pi_\mathfrak{s} F(s'+t) ds'. \end{aligned} \tag{A8}$$

It follows that

$$\partial_r \tilde{\varphi}(r) = \Pi_\mathfrak{s} F(r+t) - e^{\tau A_\mathfrak{s}} \Pi_\mathfrak{s} F(r-\tau+t) + A_\mathfrak{s} \tilde{\varphi}(r). \tag{A9}$$

Since $\tilde{\varphi}(r) = \Phi_\tau(X, t+r) - \Psi_\tau(X)$, we also have

$$\partial_r \tilde{\varphi}(r) = \partial_t \Phi_\tau(X, t+r). \tag{A10}$$

By taking the limit $r \rightarrow 0$, we obtain from (A9) and (A10) that

$$\partial_t \Phi_\tau(X, t) = \Pi_\mathfrak{s} F(t) - e^{\tau A_\mathfrak{s}} \Pi_\mathfrak{s} F(t-\tau) + A_\mathfrak{s} g_\tau(t). \tag{A11}$$

The homological Eq. (16) follows then from (A6) and (A11) while gathering the relevant terms to form the operator \mathcal{L}_A given by (17).

APPENDIX B: THE LOW-ORDER TERM IN THE OPM PARAMETERIZATION

In the special case where F in (27) is time-independent, by introducing $X_i = \langle X, e_i^* \rangle$ and $F_i = \langle F, e_i^* \rangle$, the R_n -term in the parameterization (28) takes the form

$$R_n(F, \lambda, \tau, X) = \sum_{i,j=1}^{m_c} U_{ij}^n(\tau, \lambda) B_{ij}^n F_i F_j + \sum_{i,j=1}^{m_c} V_{ij}^n(\tau, \lambda) F_j \left(B_{ij}^n + B_{ji}^n \right) X_i, \tag{B1}$$

with

$$U_{ij}^n(\tau, \lambda) = \begin{cases} \frac{1}{\lambda_i \lambda_j} \left(D_{ij}^n(\tau, \lambda) - \frac{1 - \exp(-\tau(\lambda_i - \lambda_n))}{\lambda_i - \lambda_n} - \frac{1 - \exp(-\tau(\lambda_j - \lambda_n))}{\lambda_j - \lambda_n} - \frac{1 - \exp(\tau \lambda_n)}{\lambda_n} \right) & \text{if } \lambda_i \neq 0 \text{ and } \lambda_j \neq 0, \\ \frac{1}{\lambda_i} \left(\frac{\tau \exp(-\tau(\lambda_i - \lambda_n))}{\lambda_i - \lambda_n} - \frac{1 - \exp(-\tau(\lambda_i - \lambda_n))}{(\lambda_i - \lambda_n)^2} + \frac{\tau \exp(\tau \lambda_n)}{\lambda_n} + \frac{1 - \exp(\tau \lambda_n)}{(\lambda_n)^2} \right) & \text{if } \lambda_i \neq 0 \text{ and } \lambda_j = 0, \\ \frac{1}{\lambda_j} \left(\frac{\tau \exp(-\tau(\lambda_j - \lambda_n))}{\lambda_j - \lambda_n} - \frac{1 - \exp(-\tau(\lambda_j - \lambda_n))}{(\lambda_j - \lambda_n)^2} + \frac{\tau \exp(\tau \lambda_n)}{\lambda_n} + \frac{1 - \exp(\tau \lambda_n)}{(\lambda_n)^2} \right) & \text{if } \lambda_i = 0 \text{ and } \lambda_j \neq 0, \\ \frac{\tau^2 \exp(\tau \lambda_n)}{\lambda_n} - \frac{2}{\lambda_n} \left(\frac{\tau \exp(\tau \lambda_n)}{\lambda_n} + \frac{1 - \exp(\tau \lambda_n)}{(\lambda_n)^2} \right) & \text{if } \lambda_i = 0 \text{ and } \lambda_j = 0, \end{cases} \tag{B2}$$

and

$$V_{ij}^n(\tau, \lambda) = \begin{cases} \frac{1 - \exp(-\tau(\lambda_i + \lambda_j - \lambda_n))}{\lambda_j(\lambda_i + \lambda_j - \lambda_n)} - \frac{1 - \exp(-\tau(\lambda_i - \lambda_n))}{\lambda_j(\lambda_i - \lambda_n)} & \text{if } \lambda_j \neq 0, \\ \frac{\tau \exp(-\tau(\lambda_i - \lambda_n))}{\lambda_i - \lambda_n} - \frac{1 - \exp(-\tau(\lambda_i - \lambda_n))}{(\lambda_i - \lambda_n)^2} & \text{otherwise.} \end{cases} \tag{B3}$$

For the application to the Rayleigh–Bénard system considered in Sec. V, the forcing term F is produced after rewriting the original unforced system in terms of the fluctuation variable with respect to the mean state. For this problem, the eigenvalues λ and the interaction coefficients B_{ij}^n both depend on the mean state.

APPENDIX C: NUMERICAL ASPECTS

In the numerical experiments of Sec. V, the full RB system (61) as well as the OPM reduced system (70) are numerically integrated using a standard fourth-order Runge–Kutta (RK4) method with a time-step size taken to be $\delta t = 5 \times 10^{-3}$. Note that since the eigenvalues of A are typically complex-valued, some care is needed when integrating (70). Indeed, since complex eigenmodes of A must appear in complex conjugate pairs, the corresponding components of x in (70) also form complex conjugate pairs. To prevent round-off errors that may disrupt the underlying complex conjugacy, after each RK4 time step, we enforce complex conjugacy as follows. Assuming that x_j and x_{j+1} form a conjugate pairs and that after an RK4 step, $x_j = a_1 + ib_1$ and $x_{j+1} = a_2 - ib_2$ ($i^2 = -1$) where a_1, a_2, b_1 , and b_2 are real-valued with $a_1 \approx a_2$ and $b_1 \approx a_2$, we redefine x_j and x_{j+1} to be, respectively, given by $x_j = (a_1 + a_2)/2 + i(b_1 + b_2)/2$ and $x_{j+1} = (a_1 + a_2)/2 - i(b_1 + b_2)/2$. For each component corresponding to a real eigenmode, after each RK4 time step, we simply redefine it to be its real part and ignore the small imaginary part that may also arise from round-off errors. The same numerical procedure is adopted to integrate the reduced systems obtained from invariant manifold reduction as well as the FMT parameterization used in Appendix D.

APPENDIX D: FAILURE FROM STANDARD MANIFOLD PARAMETERIZATIONS

In this section, we briefly report on the reduction skills for the chaotic case of Sec. V C as achieved through application of the

invariant manifold theory or standard formulas used in the inertial manifold theory. The invariant manifold theory is usually applied near a steady state. To work within a favorable ground for these theories, we first chose the steady state \bar{Y}_r that is closest to the mean state \bar{C}_r at the parameter value r , and we want to approximate the chaotic dynamics via a reduced system. This way, the chaotic dynamics is located near this steady state.

To derive the invariant manifold (IM) reduced system, we also re-write the RB system (61) in the fluctuation variable, but this time using the steady state \bar{Y}_r , namely, for the $\delta(t) = C(t) - \bar{Y}_r$. The analog of Eq. (64) is then projected onto the eigenmodes of the linearized part

$$\tilde{A}\delta = L\delta + B(\bar{Y}_r, \delta) + B(\delta, \bar{Y}_r) \tag{D1}$$

to obtain

$$\dot{w}_j = \lambda_j w_j + \sum_{k,\ell=1}^9 \tilde{B}_{k\ell}^j w_k w_\ell, \quad j = 1, \dots, 9. \tag{D2}$$

Here, (λ_j, f_j) denote the spectral elements of \tilde{A} , while the interaction coefficients are given as $\tilde{B}_{k\ell}^j = \langle B(f_k, f_\ell), f_j^{ast} \rangle$ with f_j^* denoting the eigenvector of \tilde{A}^* associated with λ_j^* . Note that unlike (67), there is no constant forcing term on the RHS of (D2) since $L\bar{Y}_r + B(\bar{Y}_r, \bar{Y}_r) = 0$ as \bar{Y}_r is a steady state.

Here also, the reduced state space $H_c = \text{span}(e_1, \dots, e_{m_c})$ with $m_c = 5$ as indicated in Table II, for the chaotic regime. The local IM associated with H_c has its components approximated by (Ref. 12, Theorem 2)

$$h_n(X) = \sum_{i,j=1}^{m_c} \frac{\tilde{B}_{ij}^n}{\lambda_i + \lambda_j - \lambda_n} X_i X_j, \quad n = m_c + 1, \dots, 9, \tag{D3}$$

when $\Re(\lambda_i + \lambda_j - \lambda_n) > 0$ for $1 \leq i, j \leq m_c$ and $n \geq m_c + 1$.

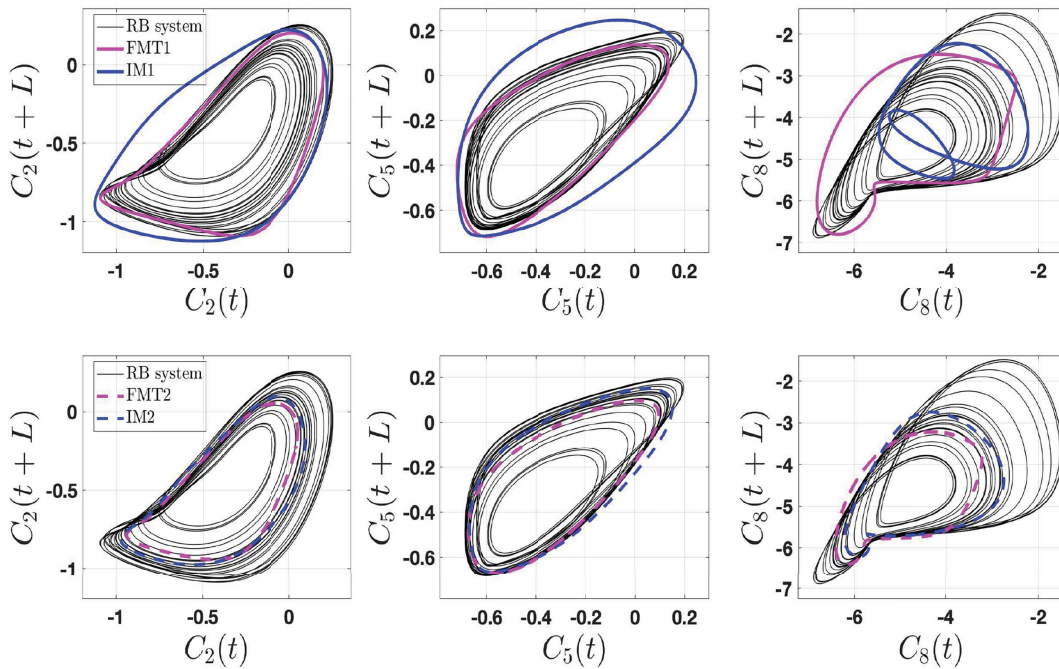


FIG. 7. The IM/FMT reduced systems are derived from Eq. (64) when the fluctuations are either taken with respect to the mean state \bar{C}_r at $r = 14.22$ [corresponding to the point P_2 in Fig. 5(d)] (bottom row) or with respect to the closest steady state to \bar{C}_r (top row). Whatever the strategy retained, the IM/FMT reduced systems fail to predict the proper chaotic dynamics, predicting instead periodic dynamics for the dimension $m_c = 5$ of the reduced state space than used for the OPM results shown in Fig. 5(B).

The corresponding IM reduced system takes the form given by (70) in which the components, Φ_ℓ , of the OPM therein are replaced by the h_ℓ given by (D3) for $\ell = m_c + 1, \dots, 9$. Unlike the OPM reduced system (70), here we use the true eigenvalues λ_j 's at the parameter r at which the dynamics is chaotic ($r = r_{P_2}$ in the notations of Fig. 5). To the solution $z(t) = (z_1(t), \dots, z_{m_c}(t))$ to this IM reduced system, one then forms the approximation $C^{IM}(t)$ of $C(t)$ given by

$$C^{IM}(t) = \sum_{j=1}^{m_c} z_j(t) f_j + \sum_{n=m_c+1}^9 h_n(z(t)) f_n + \bar{Y}_r. \quad (D4)$$

Similarly, we also test the performance of the reduced system when the local IM (D3) is replaced by the following FMT parameterization [see (30) in Remark III.2]:

$$h_n^{FMT} = - \sum_{i,j=1}^{m_c} \frac{\tilde{B}_{ij}^n}{\lambda_n} X_i X_j, \quad n = m_c + 1, \dots, 9. \quad (D5)$$

Formulas such as (D5) have been used in earlier studies relying on inertial manifolds for predicting higher-order bifurcations.⁴⁹

The predicted orbits obtained from reduced systems built either on the IM parameterization (D3) or the FMT one (D5) are shown in the top row of Fig. 7 as blue and magenta curves, respectively. Both reduced systems lead to periodic dynamics and thus fail dramatically in predicting the chaotic dynamics. The small spectral

gap issue mentioned in Remark III.1 plays a role in explaining this failure but it is not the only culprit. Another fundamental issue for the closure of chaotic dynamics lies in the difficulty to provide accurate parameterization of small-energy but dynamically important variables; see, e.g., Ref. 12, Sec. 6. This issue is encountered here, as some of variables to parameterize for Experiment II contain only from 0.23% to 2.1% of the total energy.

Replacing \bar{Y}_r by the genuine mean state \bar{C}_r does not fix this issue as some of variables to parameterize contain still a small fraction of the total energy, from 0.36% to 1.5%. The IM parameterization (D3) and the FMT one (D5) whose coefficients are now determined from the spectral elements of \tilde{A} in which \bar{C}_r replaces \bar{Y}_r in (D1), still fail in parameterizing accurately such small-energy variables; see bottom row of Fig. 7.¹¹² By comparison, the OPM succeeds in parameterizing accurately these small-energy variables. For Experiment I, inaccurate predictions are also observed from the reduced systems built either on the IM parameterization (D3) or the FMT one (D5) (not shown).

REFERENCES

- ¹But diagonalizable over the set of complex numbers \mathbb{C} .
- ²D. Henry, "Geometric theory of semilinear parabolic equations," in *Lecture Notes in Mathematics* (Springer-Verlag, Berlin, 1981), Vol. 840.
- ³M. Ghil and S. Childress, *Topics in Geophysical Fluid Dynamics: Atmospheric Dynamics, Dynamo Theory and Climate Dynamics* (Springer-Verlag, New York, 1987).

- ⁴J. K. Hale, "Asymptotic behavior of dissipative systems," in *Mathematical Surveys and Monographs* (American Mathematical Society, Providence, RI, 1988), Vol. 25, pp. x+198.
- ⁵J. D. Crawford, *Rev. Mod. Phys.* **63**, 991 (1991).
- ⁶M. C. Cross and P. C. Hohenberg, *Rev. Mod. Phys.* **65**, 851 (1993).
- ⁷G. Sell and Y. You, "Dynamics of evolutionary equations," in *Applied Mathematical Sciences* (Springer-Verlag, New York, 2002), Vol. 143, pp. xiv+670.
- ⁸T. Ma and S. Wang, "Bifurcation theory and applications," in *World Scientific Series on Nonlinear Science. Series A: Monographs and Treatises* (World Scientific Publishing, Hackensack, NJ, 2005), Vol. 53.
- ⁹P. E. Kloeden and M. Rasmussen, "Nonautonomous dynamical systems," in *Mathematical Surveys and Monographs* (American Mathematical Society, Providence, RI, 2011), Vol. 176.
- ¹⁰R. Temam, *Infinite-Dimensional Dynamical Systems in Mechanics and Physics* (Springer Science & Business Media, 2012), Vol. 68.
- ¹¹T. Ma and S. Wang, *Phase Transition Dynamics* (Springer, 2014).
- ¹²M. D. Chekroun, H. Liu, and J. C. McWilliams, *J. Stat. Phys.* **179**, 1073 (2020).
- ¹³A. J. Chorin, O. H. Hald, and R. Kupferman, *Phys. D* **166**, 239 (2002).
- ¹⁴D. Givon, R. Kupferman, and A. Stuart, *Nonlinearity* **17**, R55 (2004).
- ¹⁵G. Gottwald, *Gaz. Aust. Math. Soc.* **37**, 319 (2010).
- ¹⁶G. A. Gottwald, D. T. Crommelin, and C. L. E. Franzke, *Stochastic Climate Theory* (Cambridge University Press, 2017), pp. 209–240.
- ¹⁷V. Lucarini and M. Chekroun, [arXiv:2303.12009](https://arxiv.org/abs/2303.12009) (2023).
- ¹⁸M. D. Chekroun, H. Liu, and J. C. McWilliams, *Comput. Fluids* **151**, 3 (2017).
- ¹⁹M. D. Chekroun, H. Liu, and J. C. McWilliams, *Proc. Natl. Acad. Sci. U.S.A.* **118**, e2113650118 (2021).
- ²⁰P. Constantin, C. Foias, B. Nicolaenko, and R. Temam, *Integral Manifolds and Inertial Manifolds for Dissipative Partial Differential Equations* (Springer Science, 2012), Vol. 70.
- ²¹A. Debussche and R. Temam, *Differ. Integral Equ.* **4**, 897 (1991).
- ²²A. Debussche and R. Temam, *J. Math. Pures Appl.* **73**, 489 (1994).
- ²³R. Temam and D. Wirosoetisno, *SIAM J. Math. Anal.* **42**, 427 (2010).
- ²⁴R. Temam and D. Wirosoetisno, *J. Atmos. Sci.* **68**, 675 (2011).
- ²⁵S. Zelik, *Proc. R. Soc. Edinb. Sec. A: Math.* **144**, 1245 (2014).
- ²⁶A. Subel, Y. Guan, A. Chattopadhyay, and P. Hassanzadeh, [arXiv:2206.03198](https://arxiv.org/abs/2206.03198) (2022).
- ²⁷S. Ahmed, S. Pawar, O. San, A. Rasheed, T. Iliescu, and B. Noack, *Phys. Fluids* **33**, 091301 (2021).
- ²⁸J. Hesthaven, C. Pagliantini, and G. Rozza, *Acta Numer.* **31**, 265 (2022).
- ²⁹M. D. Chekroun, H. Liu, and S. Wang, *Stochastic Parameterizing Manifolds and Non-Markovian Reduced Equations: Stochastic Manifolds for Nonlinear SPDEs II* (Springer Briefs in Mathematics, Springer, 2015).
- ³⁰X. Cabré, E. Fontich, and R. De La Llave, *J. Differ. Equ.* **218**, 444 (2005).
- ³¹À. Haro, M. Canadell, J.-L. Figueras, A. Luque, and J.-M. Mondelo, *The Parameterization Method for Invariant Manifolds: From Rigorous Results to Effective Computations* (Springer-Verlag, Berlin, 2016), Vol. 195.
- ³²A. Roberts, [arXiv:1804.06998](https://arxiv.org/abs/1804.06998) (2018).
- ³³C. Kuehn, *Phys. D* **240**, 1020 (2011).
- ³⁴P. Ashwin, S. Wicczorek, R. Vitolo, and P. Cox, *Phil. Trans. R. Soc. A* **370**, 1166 (2012).
- ³⁵Here, we make the abuse of language that the OPM is sought within the class of parameterizations obtained through the backward–forward systems of Sec. III. In general, OPMs are more general objects related to the conditional expectation associated with the projector Π_c ; see Ref. 12, Sec. 3.2.
- ³⁶M. D. Chekroun, H. Liu, and S. Wang, *Approximation of Stochastic Invariant Manifolds: Stochastic Manifolds for Nonlinear SPDEs I*, Springer Briefs in Mathematics (Springer, 2015).
- ³⁷M. Chekroun, H. Liu, J. McWilliams, and S. Wang, *J. Differ. Equ.* **346**, 145 (2023).
- ³⁸One could also express a constraint on the behavior of $F(t)$ as $t \rightarrow \infty$. For instance, one may require that
- $$\lim_{s \rightarrow -\infty} e^{Acs} \int_s^0 e^{Acs'} \Pi_c F(s') ds' < \infty, \text{ etc.} \quad (\text{D6})$$
- ³⁹V. I. Arnold, *Geometrical Methods in the Theory of Ordinary Differential Equations*, 2nd ed. (Springer-Verlag, New York, 1988).
- ⁴⁰C. Pötzsche and M. Rasmussen, *J. Dyn. Differ. Equ.* **18**, 427 (2006).
- ⁴¹A. Dávid and S. Sinha, in *Bifurcation and Chaos in Complex Systems*, edited by J.-Q. Sun and A. C. J. Luo (Elsevier, 2006) pp. 279–338.
- ⁴²G. R. Sell, *Am. J. Math.* **107**, 1035 (1985).
- ⁴³C. Foias, O. Manley, and R. Temam, *RAIRO Modél. Math. Anal. Numér.* **22**, 93 (1988).
- ⁴⁴R. Daley, *Mon. Weather Rev.* **108**, 100 (1980).
- ⁴⁵F. Baer and J. J. Tribbia, *Mon. Weather Rev.* **105**, 1536 (1977).
- ⁴⁶B. Machenhauer, *Beitr. Phys. Atmos.* **50**, 253 (1977).
- ⁴⁷C. Leith, *J. Atmos. Sci.* **37**, 958 (1980).
- ⁴⁸A. Roberts, *ANZIAM J.* **29**, 480 (1988).
- ⁴⁹H. S. Brown, I. G. Kevrekidis, and M. S. Jolly, in *Patterns and Dynamics in Reactive Media*, edited by R. Aris, D. G. Aronson, and H. L. Swinney (Springer, 1991), pp. 11–31.
- ⁵⁰H. Stommel, *Tellus* **13**, 224 (1961).
- ⁵¹P. Cessi, *J. Phys. Oceanogr.* **24**, 1911 (1994).
- ⁵²H. A. Dijkstra, *Nonlinear Climate Dynamics* (Cambridge University Press, 2013).
- ⁵³N. Boers, *Nat. Clim. Change* **11**, 680 (2021).
- ⁵⁴T. Lenton, H. Held, E. Kriegler, J. Hall, W. Lucht, S. Rahmstorf, and H. J. Schellnhuber, *Proc. Natl. Acad. Sci. U.S.A.* **105**, 1786 (2008).
- ⁵⁵K. Bryan and F. Hansen, in *Natural Climate Variability on Decade-to-Century Time Scales* (National Academy Press, 1995), pp. 355–364.
- ⁵⁶N. Berglund and B. Gentz, *Stoch. Dyn.* **2**, 327 (2002).
- ⁵⁷Y. A. Kuznetsov, "Elements of applied bifurcation theory," 3rd ed., in *Applied Mathematical Sciences* (Springer-Verlag, New York, 2004), Vol. 112, pp. xxii+631.
- ⁵⁸O. Thual and J. McWilliams, *Geophys. Astrophys. Fluid Dyn.* **64**, 67 (1992).
- ⁵⁹H. Dijkstra and M. Molemaker, *J. Fluid Mech.* **331**, 169 (1997).
- ⁶⁰W. Weijer, H. Dijkstra, H. Oksuzoglu, F. Wubs, and A. de Niet, *J. Comput. Phys.* **192**, 452 (2003).
- ⁶¹W. Weijer, W. Cheng, S. Drijfhout, A. Fedorov, A. Hu, L. Jackson, W. Liu, E. McDonagh, J. Mecking, and J. Zhang, *J. Geophys. Res., [Oceans]* **124**, 5336, <https://doi.org/10.1029/2019JC015083> (2019).
- ⁶²P.-L. Lions, *SIAM Rev.* **24**, 441 (1982).
- ⁶³H. Kielhöfer, *Bifurcation Theory: An Introduction with Applications to Partial Differential Equations* (Springer Science & Business Media, 2011), Vol. 156.
- ⁶⁴M. D. Chekroun, *Disc. Cont. Dyn. Syst. B* **9**, 3723 (2018).
- ⁶⁵M. Ghil, *J. Atmos. Sci.* **33**, 3 (1976).
- ⁶⁶M. Ghil, in *Climatic Variations and Variability: Facts and Theories* (Springer, 1981), pp. 461–480.
- ⁶⁷G. Hetzer, in *The Mathematics of models for Climatology and Environment* (Springer, 1997), pp. 253–287.
- ⁶⁸T. Bódai, V. Lucarini, F. Lunkeit, and R. Boschi, *Clim. Dyn.* **44**, 3361 (2015).
- ⁶⁹E. Lee, S. Sasi, and R. Shivaji, *J. Math. Anal. Appl.* **381**, 732 (2011).
- ⁷⁰J. Pruiti, A. Berdahl, C. Riehl, N. Pinter-Wollman, H. Moeller, E. Pringle, L. Aplin, E. Robinson, J. Grilli, and P. Yeh *et al.*, *Phil. Trans. R. Soc. A: Biol. Sci.* **285**, 20181282 (2018).
- ⁷¹G. Bel, A. Hagberg, and E. Meron, *Theor. Ecol.* **5**, 591 (2012).
- ⁷²Y. R. Zelnik, E. Meron, and G. Bel, *Proc. Natl. Acad. Sci.* **112**, 12327 (2015).
- ⁷³J. Bebernes and D. Eberly, *Mathematical Problems from Combustion Theory* (Springer Science & Business Media, 2013), Vol. 83.
- ⁷⁴D. A. Frank-Kamenetskii, *Diffusion and Heat Exchange in Chemical Kinetics* (Princeton University Press, 2015).
- ⁷⁵Y. Du, *SIAM J. Math. Anal.* **32**, 707 (2000).
- ⁷⁶Y. Du and Y. Lou, *J. Differ. Equ.* **173**, 213 (2001).
- ⁷⁷U. Feudel, A. Pisarchik, and K. Showalter, *Chaos* **28**, 033501 (2018).
- ⁷⁸L. Caesar, S. Rahmstorf, A. Robinson, G. Feulner, and V. Saba, *Nature* **556**, 191 (2018).
- ⁷⁹A. N. Tikhonov, *Mat. Sbornik N.S.* **31**, 575 (1952).
- ⁸⁰P. Reiterer, C. Lainscsek, F. Schürer, C. Letellier, and J. Maquet, *J. Phys. A: Math. Gen.* **31**, 7121 (1998).
- ⁸¹M. D. Chekroun, J. D. Neelin, D. Kondrashov, J. C. McWilliams, and M. Ghil, *Proc. Natl. Acad. Sci.* **111**, 1684 (2014).
- ⁸²G. Gallavotti and E. Cohen, *J. Stat. Phys.* **80**, 931 (1995).
- ⁸³V. Lucarini, *J. Stat. Phys.* **173**, 1698 (2018).
- ⁸⁴W. D. McComb, A. Hunter, and C. Johnston, *Phys. Fluids* **13**, 2030 (2001).

- ⁸⁵C. Pötzsche and M. Rasmussen, *Numer. Math.* **112**, 449 (2009).
- ⁸⁶J. Jiang, Z.-G. Huang, T. P. Seager, W. Lin, C. Grebogi, A. Hastings, and Y.-C. Lai, *Proc. Natl. Acad. Sci.* **115**, E639 (2018).
- ⁸⁷J. Jiang, A. Hastings, and Y.-C. Lai, *J. R. Soc. Interface* **16**, 20190345 (2019).
- ⁸⁸E. Laurence, N. Doyon, L. J. Dubé, and P. Desrosiers, *Phys. Rev. X* **9**, 011042 (2019).
- ⁸⁹M. D. Chekroun, M. Ghil, H. Liu, and S. Wang, *Disc. Cont. Dyn. Syst. A* **36**, 4133 (2016).
- ⁹⁰M. D. Chekroun, I. Koren, and H. Liu, *Chaos* **30**, 053130 (2020).
- ⁹¹M. D. Chekroun, I. Koren, H. Liu, and H. Liu, *Sci. Adv.* **8**, eabq7137 (2022).
- ⁹²H. Held and T. Kleinen, *Geophys. Res. Lett.* **31**, L23207 (2004).
- ⁹³M. Williamson and T. Lenton, *Chaos* **25**, 036407 (2015).
- ⁹⁴S. Bathiany, M. Claussen, and K. Fraedrich, *Earth Syst. Dyn.* **4**, 63 (2013).
- ⁹⁵S. Kéfi, V. Guttal, W. Brock, S. Carpenter, A. Ellison, V. Livina, D. Seekell, M. Scheffer, E. Van Nes, and V. Dakos, *PLoS One* **9**, e92097 (2014).
- ⁹⁶M. D. Chekroun, H. Dijkstra, T. Sengul, and S. Wang, *Nonlinear Dyn.* **109**, 1887 (2022).
- ⁹⁷H. Dijkstra, T. Sengul, J. Shen, and S. Wang, *SIAM J. Appl. Math.* **75**, 2361 (2015).
- ⁹⁸D. Han, Q. Wang, and X. Wang, *Phys. D* **414**, 132687 (2020).
- ⁹⁹C.-H. Hsia, T. Ma, and S. Wang, *Z. Anal. ihre Anwend.* **27**, 233 (2008).
- ¹⁰⁰C.-H. Hsia, T. Ma, and S. Wang, *Discrete Contin. Dyn. Syst.* **28**, 99 (2010).
- ¹⁰¹C. Lu, Y. Mao, Q. Wang, and D. Yan, *J. Differ. Equ.* **267**, 2560 (2019).
- ¹⁰²T. Sengul, J. Shen, and S. Wang, *Math. Methods Appl. Sci.* **38**, 3792 (2015).
- ¹⁰³P. Berloff and J. McWilliams, *J. Phys. Oceanogr.* **29**, 1925 (1999).
- ¹⁰⁴H. Dijkstra and M. Ghil, *Rev. Geophys.* **43**, RG3002 (2005).
- ¹⁰⁵B. Nadiga and B. Luce, *J. Phys. Oceanogr.* **31**, 2669 (2001).
- ¹⁰⁶E. Simonnet, M. Ghil, K. Ide, R. Temam, and S. Wang, *J. Phys. Oceanogr.* **33**, 729 (2003).
- ¹⁰⁷E. Simonnet, M. Ghil, and H. A. Dijkstra, *J. Mar. Res.* **63**, 931 (2005).
- ¹⁰⁸V. Dakos, S. Carpenter, E. van Nes, and M. Scheffer, *Philos. Trans. R. Soc. B: Biol. Sci.* **370**, 20130263 (2015).
- ¹⁰⁹A. Majda and N. Chen, *Entropy* **20**, 644 (2018).
- ¹¹⁰H. Zhang, J. Harlim, and X. Li, *Phys. D* **427**, 133022 (2021).
- ¹¹¹G. Gottwald and S. Reich, *Phys. D* **423**, 132911 (2021).
- ¹¹²Note that here the FMT parameterization accounts for the forcing term [see Ref. 12, Eq. (4.40)] produced by fluctuations calculated with respect to \bar{C}_r .